

5. THE ARCTIC—J. Richter-Menge, M. O. Jeffries, and E. Osborne, Eds.

a. Introduction—E. Osborne, J. Richter-Menge, and M. O. Jeffries

Annual average Arctic air temperatures (above 60°N) in 2017 continued to increase at twice the rate of the rest of the world, with the annual average surface air temperature second highest (2016 ranked first) since the year 1900. Extreme warm conditions were particularly prevalent in Alaska at the end of 2017 when the atmospheric circulation drove warm southern air masses into the Pacific Arctic region.

The same wind pattern, along with high sea surface temperatures, slowed the southward advance of the sea ice edge, leading to a month-long delay in autumn freeze up in the Chukchi Sea and Bering Strait regions of the Pacific Arctic, setting another new record for the satellite era (1978–present). Earlier in the year, on 7 March, the Arctic sea ice winter maximum extent measured by satellite was the lowest on record (since 1979), covering 8% less area than the 1981–2010 mean. The 2017 sea ice minimum on 13 September was the eighth lowest on record and covered 25% less area than the long-term mean. Ten of the lowest September sea ice minimum extents have been recorded in the last eleven years. Continued loss of thick multiyear ice (evidenced by <1% multiyear ice present in March 2017 relative to 16% in 1985) also contributes a positive feedback to ice loss, as the majority of today’s sea ice is thin first-year ice prone to breakup and melt.

As summer sea ice extents continue to shrink back, seasonal buildup of upper ocean heat in ice-free regions is increasing. In August 2017, sea surface temperature (SST) records were broken for the Chukchi Sea, with some regions as warm as +11°C, or 3° to 4°C warmer than the long-term mean (1982–present). Most other boundary regions and marginal seas, which are typically ice free during summer months, also had anomalously warm SSTs in 2017. As in winter 2016/17, the delayed freeze up in the Pacific Arctic in late 2017 extended the exposure of the upper ocean in the Chukchi Sea to the sun’s heat. Mean SSTs from 1982–present show statistically significant warming trends over much of the Arctic.

After a rapid start to the Greenland ice sheet melt season in early April, moderate to below-average melt persisted for much of the remainder of the season. As a result, summertime area-averaged albedo for the entire Greenland ice sheet was the third highest value since 2000. Glaciers and ice caps outside of Greenland continue to show declining trends in cumulative mass balance. Long-term terrestrial snow cover estimates show dramatic declines in the

Arctic since 2005. In 2017, snow cover extent was again below the 1981–2010 average across the North American Arctic, driven by earlier snow melt across the Canadian Arctic.

Terrestrial permafrost, a critical component of the Arctic landscape, supports much of the built infrastructure in the region (e.g., buildings, highways, airstrips, pipelines) and continues to experience notable change. Climate variables, such as atmospheric temperature, rain events, and snow depths, are driving higher permafrost temperature and increasing active layer thickness (surface soil layer that thaws and refreezes seasonally). In 2017, five of six permafrost observatories on the North Slope of Alaska reported record warm permafrost temperatures. In the same region, tundra greening, or an increase in above-ground vegetation, has been linked to changes in the permafrost active layer thickness, the warming Arctic climate, the extended growing season, and even reductions in sea ice cover. Over the 35-year observational time series, tundra greenness has increased throughout the majority of the circumpolar Arctic, most notably on the North Slope of Alaska, Canadian low Arctic tundra, and eastern Siberia. Another phenomenon, tundra browning, is emerging in the relatively sparse regions of western Alaska, the Canadian Archipelago high Arctic, and northwestern Siberia and may be attributed to winter warming events and perhaps even insect outbreaks. The Arctic tundra is also impacted by wildland fires, which are increasing as a result of warming climate conditions. While 2017 was an average wildfire season in Alaska (652 904 acres burned), significantly warmer and drier conditions in the Upper Yukon zone of northeast Alaska resulted in high fire danger for much of the season and accounted for more than half of the acres burned in the United States.

High above the Arctic, atmospheric ozone concentrations in winter 2016/17 were unremarkable and well above previous record minima in 2010/11 and 2015/16. UV radiation, which depends on atmospheric ozone concentrations and other factors, varied in time and space across the Arctic.

While observational time series are central to monitoring Arctic change, paleoclimate reconstructions based on fossil records can help scientists place the rates and magnitudes of modern change into a long-term, geological context. Arctic paleoceanographic records indicate that the magnitude and sustained rate of declining sea ice trend observed in the modern era is unprecedented in any existing high resolution paleoclimate sea ice reconstruction for at least the last 1450 years. Similarly, according

to paleoclimate studies, today's abnormally warm Arctic air and sea surface temperatures have not been observed in the last 2000 years. Indigenous knowledge gathered by Arctic Peoples over many millennia is another means to holistically understand Arctic change beyond instrumental records. Coproduction of knowledge can bring together knowledge systems of scientists and indigenous knowledge-holders to develop suitable sustainability and adaptation practices to address issues arising from the changing Arctic system (see Sidebar 5.2).

b. Surface air temperature—J. Overland, E. Hanna, I. Hanssen-Bauer, S.-J. Kim, J. E. Walsh, M. Wang, U. S. Bhatt, and R. L. Thoman

Arctic surface air temperature is an indicator of both regional and global climate change. Although natural variability contributes to year-to-year and regional differences in air temperature, the magnitude of the long-term temperature trend across the entire Arctic is an indicator of global climate change and the impact of increasing greenhouse gas concentrations (Overland 2009; Notz and Stroeve 2016).

After a warm Arctic-wide autumn 2016, early 2017 had notable short-term, regional temperature anomalies in response to a highly variable jet stream. Spring and summer 2017 had near-average air temperatures relative to the 1981–2010 climatology. The spring and summer conditions were reminiscent of those occurring before the long-term, above-average temperature increases began in the 1990s. Rather than higher sea level pressure extending over much of the Arctic, as observed in many recent years, weak low pressures were seen in 2017—a return to a wind forcing typical from a decade ago. The atmospheric forcing in spring and summer 2017 is consistent with a year when some Arctic indicators ran counter to the recent long-term trend over the previous decade. For example, Eurasian spring snow extent was above average for the first time in over a decade (see Section 5i).

At +1.6°C, the mean annual 2017 surface air temperature (SAT) anomaly for land stations north of 60°N is the second highest value (after 2016) in the record starting in 1900 (Fig. 5.1). Despite near-average temperatures during spring and summer months, extreme heat during autumn and winter, particularly over the Chukchi Sea and extending northward to the pole, contributed to near-record breaking warm conditions in 2017 (Fig. 5.2). Currently, the Arctic is warming at more than twice the rate of lower latitudes.

The greater rate of Arctic temperature increase, compared to the global increase, is referred to as

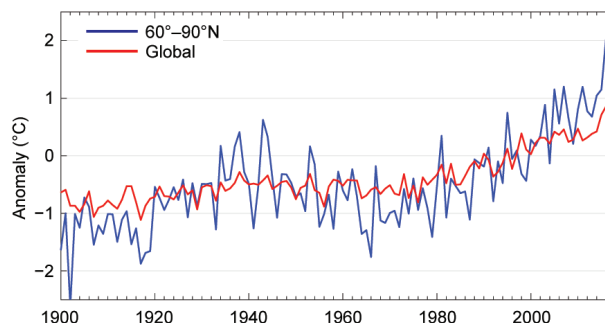


FIG. 5.1. Arctic (land stations north of 60°N) and global mean annual land surface air temperature (SAT) anomalies (°C, 1981–2010 base period) for 1900–2017. Note that there were few stations in the Arctic, particularly in northern Canada, before 1940. (Source: CRUTEM4 dataset.)

Arctic amplification. Mechanisms for Arctic amplification include: reduced summer albedo due to losses of sea ice and snow cover; the increase of total water vapor content in the Arctic atmosphere; a summer decrease and winter increase in total cloudiness (Makshtas et al. 2011); the additional heat generated by newly sea ice-free ocean areas that are maintained later into the autumn (Serreze and Barry 2011); and the lower rate of heat loss to space in the Arctic,

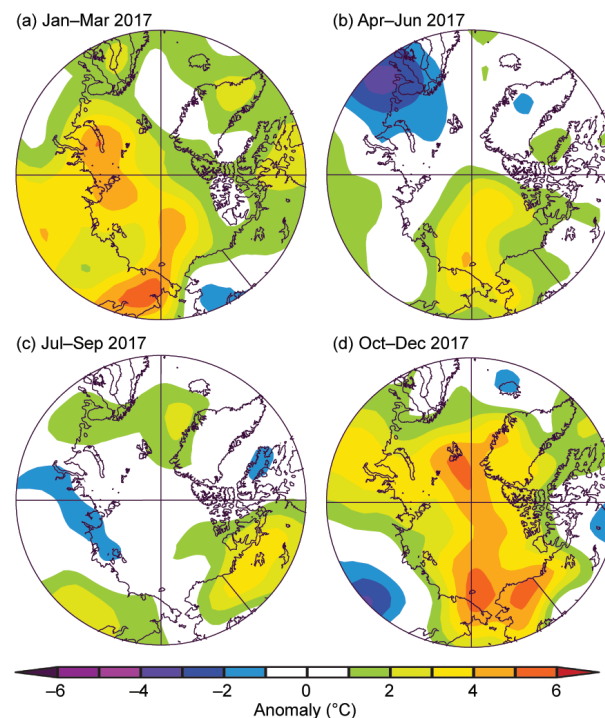


FIG. 5.2. Seasonal anomaly patterns for near-surface air temperatures (°C, 1981–2010 base period) for 2017 in (a) JFM, (b) AMJ, (c) JAS, and (d) OND. Temperatures are from slightly above the surface layer (925 mb) to emphasize large spatial patterns rather than local features. (Source: NOAA/ESRL.)

relative to the subtropics, due to lower mean surface temperatures in the Arctic (Pithan and Mauritsen 2014). Recent reductions in air pollution in Europe are reducing the relative rate of Arctic warming due to decreased downward longwave radiation, countering other mechanisms that contribute to Arctic amplification (Acosta Navarro et al. 2016).

Seasonal air temperature variations in 2017 are divided into winter (January–March, JFM), spring (April–June, AMJ), summer (July–September, JAS), and autumn (October–December, OND; Fig. 5.2). These seasonal SAT divisions are chosen to coincide with the seasonal cycles of key Arctic variables. For example, the summer sea ice minimum occurs in September, and autumn cooling continues through December.

On a seasonal basis, winter was unremarkable in terms of major features (Fig. 5.2a). However, there were notable short-term, regional temperature anomalies in response to highly variable jet stream shapes. For instance, Iceland experienced a record high maximum temperature of 19.1°C in February, exceeding the previous February (1998) record of 18.1°C by a full degree (Trausti Jonsson, Icelandic Met Office, 2017, personal communication). March 2017 had major warmth across Siberia (Fig. 5.3) including eastern Asia.

Spring showed some positive temperature anomalies in the East Siberian Sea (Fig. 5.2b), a continuation

of a warm feature observed in March. This regional warming supported early sea ice loss in the Chukchi Sea (see Section 5d). May saw anomalous high pressure extend between Greenland and Norway, with relatively warm but unexceptional temperatures over Greenland.

Similar to summer 2016, neutral temperature anomalies occurred across the central Arctic in summer 2017 (Fig. 5.2c), in contrast to the warm conditions observed during much of the previous decade. The summer 2017 conditions did not support continued overall extreme summer sea ice loss (see Section 5d). Mean coastal Greenland temperatures were near climatological levels, in contrast to some summers in the recent decade.

Alaska/northwestern Canada was the only region with above-average summer surface air temperatures. Several locations in the interior of Alaska had the warmest calendar month of record in July. On a more local and short-term basis, many stations in the north and east of Iceland reported record high temperatures for September.

Summer sea level pressure was characterized by negative anomalies in the central Arctic (Fig. 5.4). This pattern prevented extra heat in the midlatitudes from penetrating into the central Arctic. Such added heat from outside the Arctic is associated with low sea ice summers (Parkinson and Comiso 2013). This sea level pressure pattern was accompanied by cloud

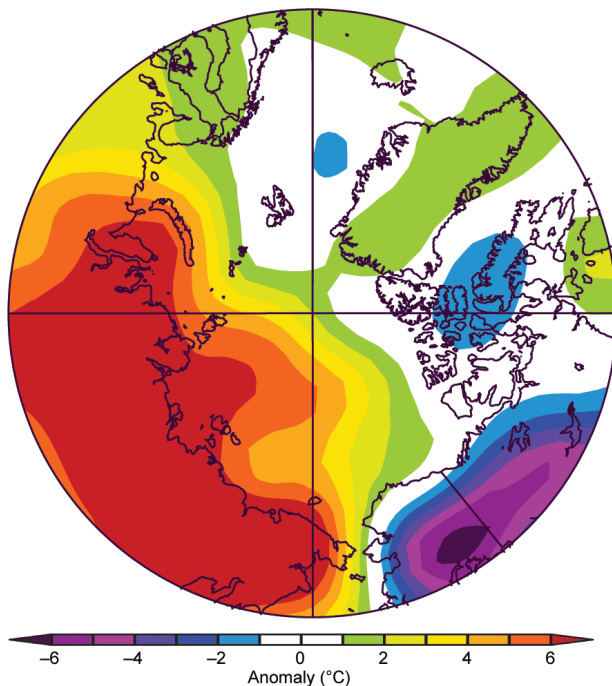


FIG. 5.3. Arctic Mar 2017 air temperature anomalies (°C).

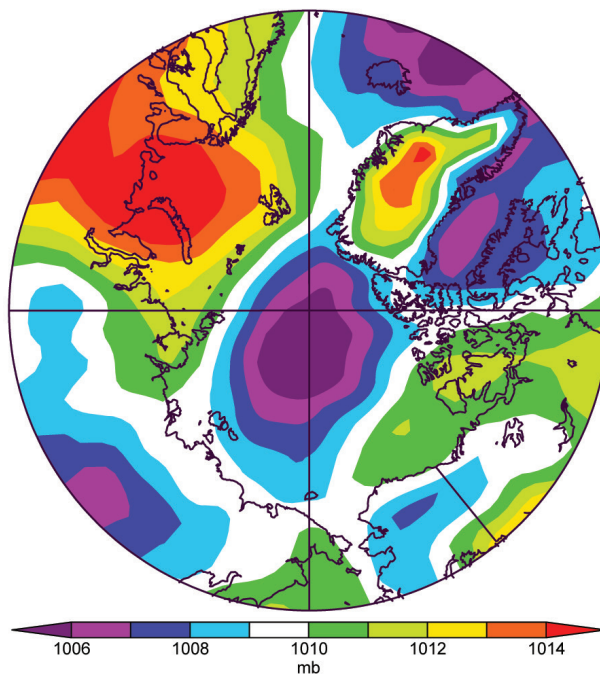


FIG. 5.4. Arctic mean sea level pressure field (hPa) for summer 2017.

cover that limited the solar heating of the lower atmosphere in the central Arctic.

A broad swath of extreme warm temperature anomalies ($> +4^{\circ}\text{C}$) stretched across the central Arctic in autumn (Fig. 5.2d). The warmest temperature extremes, north of the Bering Strait and north of Svalbard, were due to heat stored in the upper Arctic Ocean (see Section 5c) and to advection of warm air from the south (generated from the Pacific and Atlantic Oceans).

December 2017 had extreme warm temperatures in Alaska and cold temperatures in the central and eastern U.S., with incidences of snow as far south as Mississippi (Fig. 5.5a). This temperature pattern is associated with large north–south meanders of the tropospheric jet stream (Fig. 5.5b). Because the extratropical mid-troposphere wind direction approximately follows the contour direction of geopotential heights, Fig. 5.5b shows warm winds from the southwest extending into Alaska and cold air moving southeast from Canada in December. Warm air is less dense and supports rising geopotential heights. Thus,

warm temperatures over Alaska can help maintain the persistence of this North American weather pattern. Contributing to the relatively warm temperatures in Alaska in autumn was the delayed freeze-up of sea ice in Alaskan waters. Freeze-up lasted well into December and set a new record for the satellite era beginning in 1978 (see Section 5d).

c. Sea surface temperature—M.-L. Timmermans, C. Ladd, and K. Wood

Summer sea surface temperatures (SST) in the Arctic Ocean are determined mainly by absorption of solar radiation into the surface layer. In the Barents and Chukchi Seas, there is an additional contribution from advection of warm water from the North Atlantic and North Pacific Oceans, respectively. Solar warming of the ocean surface layer is influenced by the distribution of sea ice (with more solar warming in ice-free regions), cloud cover, water color, and upper-ocean stratification. River influxes influence the latter two, as well as provide an additional source of warm water. SSTs are an essential indicator of the role of the ice–albedo feedback mechanism in any given melt season; as the area of sea ice cover decreases, more incoming solar radiation is absorbed by the ocean and the warmer ocean in turn melts more sea ice.

SST data presented here are from the NOAA Optimum Interpolation (OI) SST Version 2 product (OISSTv2), which is a blend of in situ and satellite measurements (Reynolds et al. 2002, 2007). Compared to in situ temperature measurements, the OISSTv2 product showed average correlations of about 80%, with an overall cold SST bias of -0.02°C (Stroh et al. 2015).

August SSTs provide the most appropriate representation of Arctic Ocean summer SSTs because they are not affected by the cooling and subsequent sea ice growth that typically takes place in the latter half of September. Mean SSTs in August 2017 in ice-free regions ranged from $\sim 0^{\circ}\text{C}$ in some regions to as high as 11°C in the Chukchi and Barents Seas (Fig. 5.6a). Compared to the 1982–2010 August mean (note the monthly SST record begins in December 1981), most boundary regions and marginal seas had anomalously high SSTs in August 2017 (Fig. 5.6b). Particularly high anomalies (around $3^{\circ}\text{--}4^{\circ}\text{C}$ above the 1982–2010 average) were observed in the Beaufort, Chukchi, and southern Barents Seas. SSTs in the boundary regions and marginal seas, which are mostly ice free in August, are linked to the timing of local sea ice retreat, which facilitates the direct solar heating of the exposed surface waters.

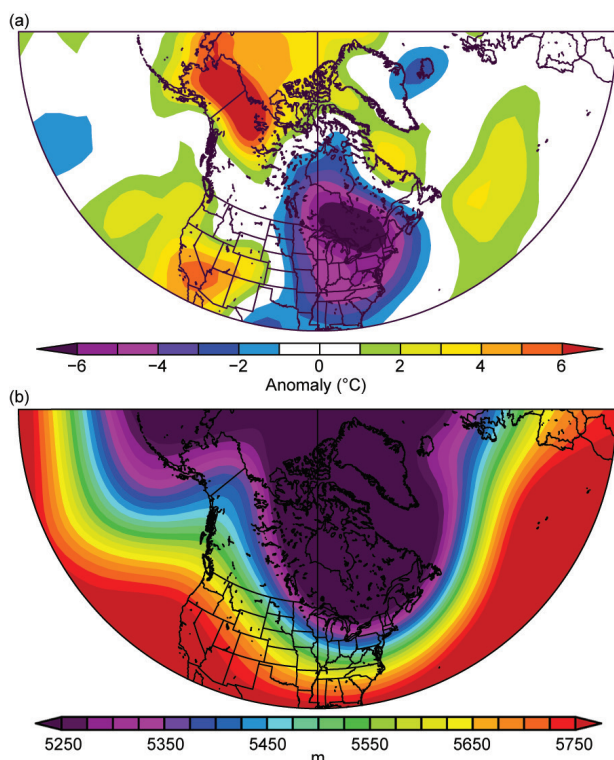


FIG. 5.5. Dec 2017 fields show the cause of warm temperatures in Alaska and simultaneous cold temperatures in the central and southern U.S. (a) 925-hPa air temperature anomalies ($^{\circ}\text{C}$) and (b) corresponding 500-hPa geopotential height field (m), showing the strong wave tropospheric jet stream pattern extending north into Alaska and south into eastern North America.

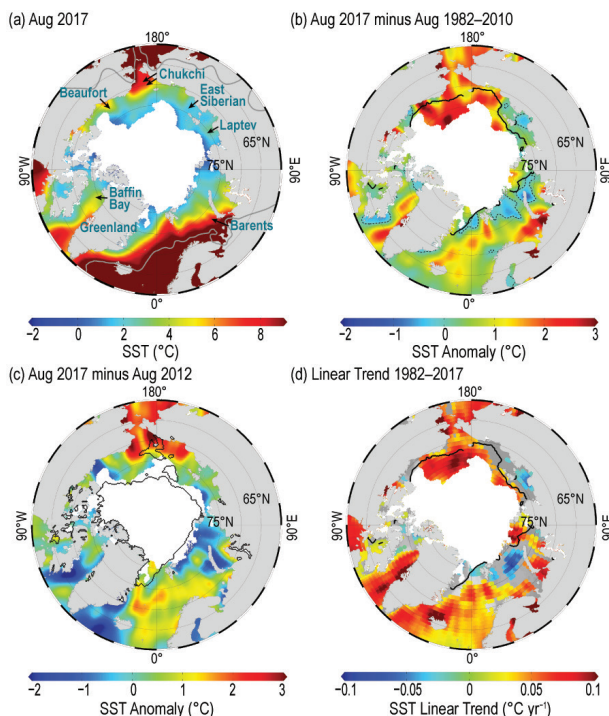


FIG. 5.6. (a) Mean SST ($^{\circ}\text{C}$) in Aug 2017. White shading is the Aug 2017 mean sea ice extent (shown in each panel) and gray contours indicate the 10°C SST isotherm. (b) SST anomalies ($^{\circ}\text{C}$) in Aug 2017 relative to the Aug 1982–2010 mean (dotted black contour indicates zero anomaly). Black line indicates the median ice edge for Aug 1982–2010. (c) SST anomalies ($^{\circ}\text{C}$) in Aug 2017 relative to Aug 2012. Black line indicates the median ice edge for Aug 2012. (d) Linear SST trend ($^{\circ}\text{C yr}^{-1}$) for Aug of each year from 1982–2017. Trend is only shown for values that are significant at the 95% confidence interval; the region is gray otherwise. Black line indicates the median ice edge for Aug 1982–2010. (Sources: SST data are from the NOAA OISSTv2; sea ice extent and ice-edge data are from NSIDC Sea Ice Index, Version 3, Fetterer et al. 2017.)

In August, regions off the west and east coasts of Greenland and in the southern Barents Sea were markedly cooler (by up to 3°C) than in August 2016 (see Timmermans 2017). It is notable also that compared to August 2012 (the summer of lowest minimum sea ice extent in the satellite record, 1979–present), August 2017 SSTs in the Chukchi Sea region were up to 3°C higher (Fig. 5.6c). This illustrates the significant interannual and spatial variability in summer SSTs. Cooler SSTs in August 2012 (compared to August 2017) in the Chukchi Sea were related to the persistence of sea ice in that particular region (even while the main ice pack retreated) and a strong cyclonic storm in the region that brought cool conditions late in the summer season (see Timmermans et al. 2013).

Mean August SSTs from 1982 to 2017 show statistically significant linear warming trends over much

of the Arctic Ocean (Fig. 5.6d); the cooling trends in the Laptev and northern Barents Seas are notable exceptions. Warming trends coincide with declining trends in summer sea ice extent (including late-season freeze-up and early melt, e.g., Parkinson 2014; see section 5d), increased solar absorption (e.g., Pinker et al. 2014), release of stored ocean heat (e.g., Timmermans 2015), and milder air temperatures (see Section 5b). Mean August SSTs for the entire Chukchi Sea region exhibit a statistically significant warming trend of about $+0.7^{\circ}\text{C decade}^{-1}$, based on a linear fit.

d. Sea ice cover—D. Perovich, W. Meier, M. Tschudi, S. Farrell, S. Hendricks, S. Gerland, C. Haas, T. Krumpen, C. Polashenski, R. Ricker, and M. Webster

1) SEA ICE EXTENT

Arctic sea ice (1) acts as a barrier between the underlying ocean and the atmosphere, (2) limits the amount of absorbed solar energy due to its high albedo, (3) provides a habitat for biological activity, and (4) limits human access to the Arctic Ocean and adjacent seas. The extent of the Arctic sea ice cover varies substantially over the course of a year, with the end-of-winter ice cover generally two to three times as large as at the end of summer. The months of March and September are of particular interest because they are the months when the sea ice typically reaches its maximum and minimum extents, respectively. Figure 5.7 shows the monthly average Arctic sea ice extents in March 2017 and September 2017, measured by satellite-based passive microwave instruments.

Sea ice extent is the total area covered by at least 15% concentration of sea ice. Based on data from the

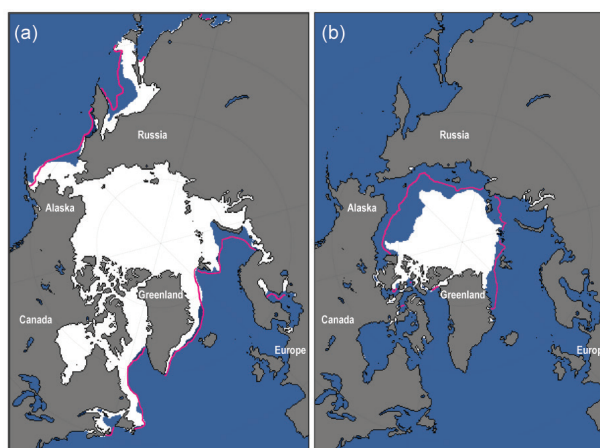


FIG. 5.7. Average monthly sea ice extent in (a) Mar (left) and (b) Sep (right) 2017 illustrate the respective winter maximum and summer minimum extents. The magenta line indicates the median ice extents in Mar and Sep, respectively, for the period 1981–2010. Maps are from NSIDC at https://nsidc.org/data/seaice_index (Fetterer et al. 2017).

National Snow and Ice Data Center (NSIDC) sea ice index (Fetterer et al. 2017), the sea ice cover reached a maximum extent of 14.42 million km² on 7 March, which was 8% below the 1981–2010 average. This is the lowest maximum value ever observed in the satellite record.

On 13 September, the sea ice extent reached a summer minimum value of 4.64 million km². This is the eighth lowest extent in the satellite record. While the 2017 minimum extent represents a modest increase from the 2016 minimum, it was 25% less than the 1981–2010 average minimum ice extent. The 10 lowest September extents have occurred in the last 11 years (Parkinson and DiGirolamo 2016).

In 2017, sea ice extent showed decreasing trends in all months and virtually all regions, except for the Bering Sea during winter (Meier et al. 2014). The September (typical Arctic sea ice minimum) monthly average trend for the entire Arctic Ocean is now -13.2% decade⁻¹ relative to the 1981–2010 average (Fig. 5.8). Trends are smaller during March (typical Arctic sea ice maximum), at -2.7% decade⁻¹, but the decrease is statistically significant. Both the September and March trends are significant at the 99% confidence level.

Freeze-up in the Chukchi Sea was extremely slow, and the sea ice extent in the region at the beginning of December 2017 was the lowest in the satellite record. It was not until the end of December that the region was substantially frozen over, a month later than normal. Upper ocean heat accumulated during the summer, through the absorption of solar radiation, likely slowed ice growth in the Chukchi

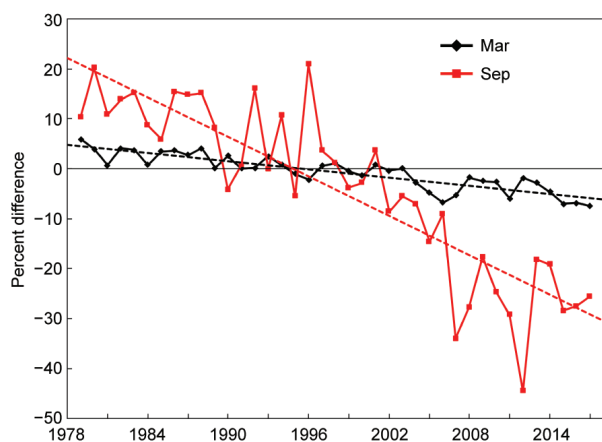


FIG. 5.8. Time series of sea ice extent anomalies (%) in Mar (the month of maximum ice extent) and Sep (the month of minimum ice extent). Anomaly value for each year is the percent difference in ice extent relative to the 1981–2010 mean. The black and red dashed lines are least squares linear regression lines.

region (see Section 5c). Anomalous southerly winds during October–December also played a significant role by advecting warm air and ocean waters into the region through the Bering Strait (see Section 5b) and preventing southward advancement of the ice edge.

2) AGE OF THE ICE

The age of sea ice is another key descriptor of the state of the sea ice cover. Compared to younger ice, older ice tends to be thicker, stronger, and more resilient to changes in atmospheric and oceanic forcing (i.e., changes in atmospheric circulation patterns and ocean heat). The age of the ice is measured using satellite observations and drifting buoy records to track ice parcels over several years (Tschudi et al. 2010; Maslanik et al. 2011). This method has been used to provide a record of the age of the ice since 1985 (Tschudi et al. 2015, 2016).

Very old ice (>4 years old) continues to be a diminishingly small fraction of the Arctic ice pack in March (Fig. 5.9). The extent of the oldest ice has declined from 2.54 million km² in March 1985 (representing 16% of the total ice pack) to 0.13 million km² in March 2017 (0.9% of the total ice pack). The distribution of ice age in March 2017 was similar to that of March 2016, although there was a decrease in the fractional coverage of the oldest ice, from 1.2% in March 2016 to 0.9% in March 2017. First-year ice dominates the winter sea ice cover, comprising ~79% of the ice cover

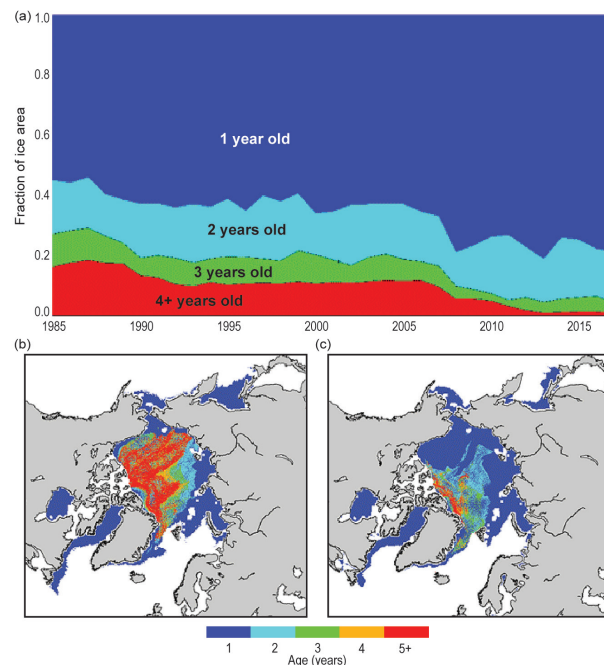


FIG. 5.9. (a) Arctic sea ice age coverage by year, expressed as the fraction of the total ice area, 1985–2017. Sea ice age coverage maps for (b) Mar 1985 and (c) Mar 2017.

in March 2017, compared to ~55% in the 1980s. The thinner, younger ice is more mobile and susceptible to mechanical wind forcing, and it is vulnerable to complete melting in the summer and contributes to the observed decrease in summer sea ice extents by enabling more heat to be absorbed by the upper ocean.

3) SEA ICE THICKNESS AND SNOW DEPTH

Satellite remote sensing and regular airborne survey programs continued to record changes in Arctic sea ice thickness and volume. These survey programs derive ice thickness and volume by observing the freeboard of the ice cover, which is the distance between the surface of the ocean and the top of the ice. During this past year the ESA *CryoSat-2* radar altimeter mission completed its seventh year of operation, providing sea ice thickness estimates between October and April (Laxon et al. 2013). The *CryoSat-2* freeboard measurements expand the data record of satellite and submarine-based observations that document the decline in sea ice thickness since 1958 (Kwok and Rothrock 2009; Lindsay and Schweiger 2015).

In spring 2017, *CryoSat-2* products from the Alfred Wegener Institute indicated a spatially variable pattern of ice thickness (Fig. 5.10a), which is typical. The April 2017 thickness anomaly, compared to the period 2011–16 (Fig. 5.10b), shows below-average thicknesses in the multiyear ice region north of the Queen Elizabeth Islands of the Canadian Arctic Archipelago, the Chukchi Sea, and the shelf regions of the East Siberian Sea. Above-average thicknesses were observed in the Beaufort Sea and the eastern part of the central Arctic Ocean.

Sea ice volume estimates were generated from *Cryosat-2* observations for 2011–17 for the months of October through April. Results for the central Arctic Ocean show a decline from 2011 to 2013, an increase in 2014, followed by a steady decline from 2014 to 2017. The April 2017 sea ice volume ($13.19 \pm 1.15 \times 10^3 \text{ km}^3$) ranks as the third lowest spring volume after April 2012 ($13.14 \pm 1.27 \times 10^3 \text{ km}^3$) and 2013 ($12.56 \pm 1.21 \times 10^3 \text{ km}^3$) in the *CryoSat-2* data record (2011–17). The difference between the three lowest volume estimates lies within the observational uncertainties of the instrument. For more information regarding instrument uncertainty see Ricker et al. (2014).

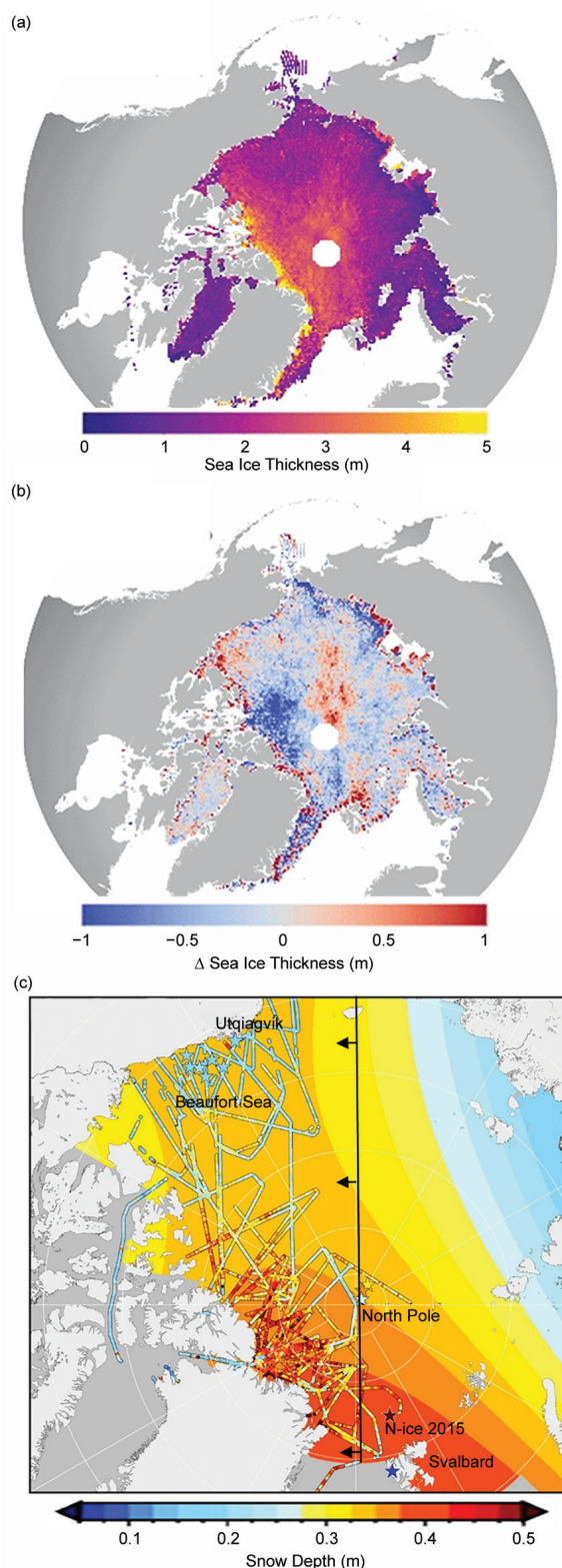


FIG. 5.10. Apr 2017 (a) sea ice thickness (m) derived from *CryoSat-2* radar altimeter data and (b) sea ice thickness anomaly (m; base period 2011–16). (c) Snow depth (m) on Arctic sea ice at the end of winter, prior to melt onset; recent in situ measurements (stars), made in 2015 and 2017, and airborne observations (multiple airborne survey lines), made in Mar and May in 2009–12 and 2014–15, are overlaid on the long term mean snow depth for the months of Mar and Apr (adapted from Warren et al. 1999). Black line and arrows in (c) designate the western Arctic.

SIDEBAR 5.1: PALEOCLIMATE RECORDS: PROVIDING CONTEXT AND UNDERSTANDING OF CURRENT ARCTIC CHANGE— E. OSBORNE, T. CRONIN, AND J. FARMER

At present, the Arctic Ocean is experiencing changes in ocean surface temperature and sea ice extent that are unprecedented in the era of satellite observations, which extend from the 1980s to the present (see Sections 5c,d). To provide context for current changes, scientists turn to paleoclimate records to document and study anthropogenic influence and natural decadal and multidecadal climate variability in the Arctic system. Paleoceanographic records extend limited Arctic instrumental measurements back in time and are central to improving our understanding of climate dynamics and the predictive capability of climate models. By comparing paleoceanographic records with modern observations, scientists can place the rates and magnitudes of modern Arctic change in the context of those inferred from the geological record.

Over geological time, paleoceanographic reconstructions using, for instance, marine sediment cores indicate that the Arctic has experienced huge sea ice fluctuations. These fluctuations range from nearly completely ice-free to totally ice-covered conditions. The appearance of ice-

rafted debris and sea ice-dependent diatoms in Arctic marine sediments indicate that the first Arctic sea ice formed approximately 47 million years ago (St. John 2008; Stickley et al. 2009; Fig. SB5.1), coincident with an interval of declining atmospheric carbon dioxide (CO_2) concentration, global climate cooling, and expansion of Earth's cryosphere during the middle Eocene. The development of year-round (i.e., perennial) sea ice in the central Arctic Ocean, similar to conditions that exist today, is evident in sediment records as early as 14–18 million years ago (Darby 2008). These records suggest that transitions in sea ice cover occur over many millennia and often vary in concert with the waxing and waning of circum-Arctic land ice sheets, ice shelves, and long-term fluctuations in ocean and atmosphere temperatures and atmospheric CO_2 concentrations (Stein et al. 2012; Jakobsson et al. 2014).

Over shorter time scales, shallow sediment records from Arctic Ocean continental shelves allow more detailed, higher-resolution (hundreds of years resolution) reconstructions of sea ice history extending through the Holocene (11 700 years ago to present), the most recent interglacial period.

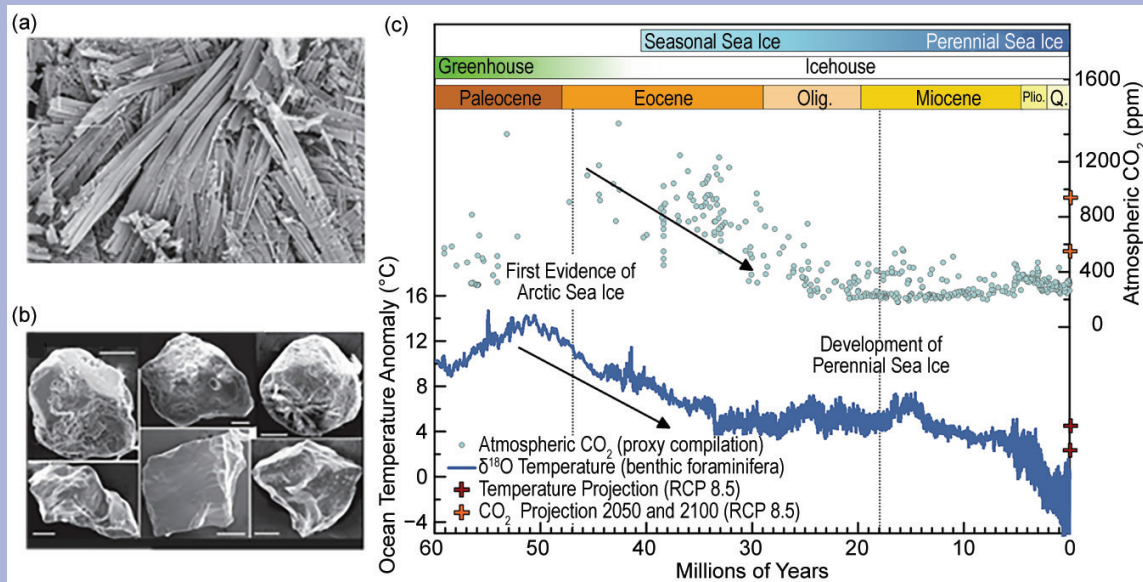


FIG. SB5.1. The oldest known paleoclimate evidence of sea ice in the Arctic are (a) fossilized remains of sea ice dwelling diatoms (*Synedropsis* spp.) and (b) ice rafted debris that date back to 47 million years ago (Stickley et al. 2009). (c) Global compilation of paleoclimate records indicates that cooling ocean temperatures (°C) and declining atmospheric CO_2 (ppm) coincide with major NH sea ice development (data: Beerling and Royer 2011; Zhang et al. 2013; Anagnostou et al. 2016). Global ocean temperature anomalies are determined by millions of stable oxygen isotopic measurements of fossilized calcite benthic foraminifera shells. Arrows indicate cooling temperature and declining CO_2 concentrations through the greenhouse to icehouse transition. Red and orange “+” on the right y-axis indicate the CMIP5 multimodel mean projected temperature and atmospheric CO_2 , respectively, in the year 2050 and 2100.

A notable feature of these records is an early Holocene sea ice minimum, corresponding to a thermal maximum (warm) period from 11 000 to 5000 years ago, when the Arctic may have been warmer and had less summertime sea ice than today (Kaufman et al. 2004). However, it is not clear that the Arctic was ice-free at any point during the Holocene (Polyak et al. 2010). High-resolution paleo–sea ice records from the western Arctic in the Chukchi and East Siberian Seas indicate that sea ice concentrations increased through the Holocene in concert with decreasing summer solar insolation (sunlight). Sea ice extent in this region also varied in response to the volume of Pacific water delivered via the Bering Strait into the Arctic Basin (Stein et al. 2017; Polyak et al. 2016). Records from the Fram Strait (Müller et al. 2012), Laptev Sea (Hörner et al. 2016), and Canadian Arctic Archipelago (Vare et al. 2009) also indicate a similar long-term expansion of sea ice and suggest sea ice extent in these regions is modulated by the varying influx of warm Atlantic water into the Arctic Basin (e.g., Werner et al. 2013). Taken together, available records support a circum-Arctic sea ice expansion during the late Holocene.

A notably high-resolution summer sea ice history (<5-year resolution) has been established for the last 1450 years using a network of terrestrial records (tree ring, lake sediment, and ice core records) located around the margins of the Arctic Ocean (Kinnard et al. 2011). Results summarized in Fig. SB5.2 indicate a pronounced decline in summer sea ice extent beginning in the 20th century, with exceptionally low ice extent recorded since the mid-1990s, consistent with the satellite record (see Section 5d). While several episodes of reduced and expanded sea ice extent occur in association with climate anomalies such as the Medieval Climate Warm Period (AD 800–1300) and the Little Ice Age (AD 1450–1850), the magnitude and pace of the modern decline in sea ice is outside of the range of natural variability and unprecedented in the 1450-year reconstruction (Kinnard et al. 2011). A radiocarbon-dated driftwood record of the Ellesmere ice shelf in the Canadian High Arctic, the oldest landfast ice in the Northern Hemisphere, also demonstrates a substantial reduction in ice extents over the 20th century (England et al. 2017). A supporting sediment record indicates that inflowing Atlantic water in Fram Strait has warmed by 2°C since 1900, driving break up and melt of sea ice (Spielhagen et al. 2011). Complementary mooring and satellite observations show the “Atlantification” of the eastern Arctic due to enhanced inflow of warm saline water through Fram Strait (Nilsen et al. 2016) and nutrient-rich Pacific water via the Bering has increased by more than 50%

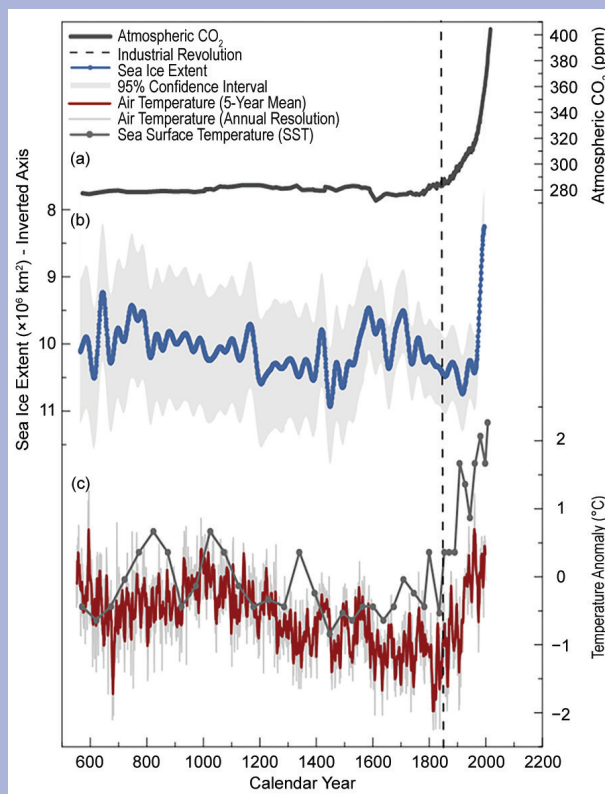


FIG. SB5.2. (a) Atmospheric CO₂ concentrations (ppm), (b) paleoclimate reconstructions of summer Arctic sea ice extent (km²; Kinnard et al. 2011), and (c) annual atmospheric temperature anomalies (°C; McKay and Kaufman 2014) and sea surface temperature anomalies (°C; Spielhagen et al. 2011) spanning the last 1500 years. Atmospheric (red solid line: 5-yr mean and light gray: annual mean) and upper-ocean (dark gray with circles indicating individual data points) temperature anomalies are plotted together to show respective temperature trends. Vertical dashed line indicates the onset of the Industrial Revolution. Atmospheric CO₂ concentrations [shown in (a)] are from the Law Dome ice core record (Etheridge et al. 1996, 1998) and modern observations from the Mauna Loa observatory [Dr. Pieter Tans, NOAA/ESRL (www.esrl.noaa.gov/gmd/ccgg/trends/)], and Dr. Ralph Keeling, Scripps Institution of Oceanography (www.scrippsco2.ucsd.edu/)].

(Woodgate et al. 2012), further driving sea ice melt and warming seas. Similar high-resolution proxy records from Arctic regions also indicate that the modern rate of increasing annual surface air temperatures has not been observed over at least the last 2000 years (McKay and Kaufman 2014). Scientists conclude that broad-scale sea ice variations recorded in the paleo

CONT. SIDEBAR 5.1: PALEOCLIMATE RECORDS: PROVIDING CONTEXT AND UNDERSTANDING OF CURRENT ARCTIC CHANGE— E. OSBORNE, T. CRONIN, AND J. FARMER

record were predominantly driven by changes in basin-scale atmospheric circulation patterns, fluctuations in air temperature and strength of incoming solar radiation, and changes in the inflow of warm water via Pacific and Atlantic inflows (Polyak et al. 2010).

There is general consensus that ice-free Arctic summers are likely before the end of the 21st century (e.g., Stroeve et al. 2007; Massonnet et al. 2012), while some climate model projections suggest ice-free Arctic summers as early as 2030 (Wang and Overland 2009). Paleoclimate

Snow plays several critical roles in the growth and melt of Arctic sea ice. These roles include insulating the ocean from the atmosphere, dampening heat fluxes, reducing sea ice growth, reflecting more than 80% of the incoming sunlight, delaying ice melt, and contributing to melt pond formation (Granskog et al. 2017). Prior to the 1990s, observations of snow on Arctic sea ice were limited to in situ measurements. Warren et al. (1999) compiled many of these observations into a long-term record. New approaches to measure snow depth have since emerged, including improved instruments for in situ and autonomous observations and remote sensing. Field observations from recent years underscore significant regional and interannual variability in snow on Arctic sea ice. Figure 5.10c shows the historical snow depth record, plus a compilation of airborne snow depth measurements collected between March and May in 2009–12 and 2014–15, and in situ measurements made in 2015 and 2017. The recent mean snow depths range from 0.05 to 0.55 m. Compared to the record published by Warren et al. (1999) there has been an overall decrease in snow depths of $37\% \pm 29\%$ in most of the western Arctic (aka North American Arctic) at the end of winter (Fig. 5.10c). The trend in the mean anomalies is -0.27 cm yr^{-1} with 99% significance. This decrease is potentially associated with later sea ice formation and thus later onset of snow accumulation in the previous autumn (Webster et al. 2014; Kurtz and Farrell 2011; Blanchard-Wrigglesworth et al. 2015).

e. *Greenland ice sheet*—M. Tedesco, J. E. Box, J. Cappelen, R. S. Fausto, X. Fettweis, K. Hansen, M. S. Khan, S. Luthcke, T. Mote, I. Sasgen, C. J. P. P. Smeets, D. van As, R. S. W. van de Wal, and I. Velicogna

The Greenland ice sheet (GrIS) plays a crucial role in the climatological, hydrological, and ecological

studies and observational time series attribute the decline in sea ice extent and thickness over the last decade to both enhanced greenhouse warming and natural climate variability. While understanding the interplay of these factors is critical for future projections of Arctic sea ice and ecosystems, most observational time series records cover only a few decades. This highlights the need for additional paleoceanographic reconstructions across multiple spatial and temporal domains to better understand the drivers and implications of present and future Arctic Ocean change.

cycles at regional and global scales. The high albedo of the ice sheet contributes to a modulation of the amount of solar energy absorbed by Earth, and the location and topography of the ice sheet affects atmospheric circulation. The GrIS is also a major contributor to current and projected sea level rise, through surface runoff and iceberg calving. The summer of 2017 over the Greenland ice sheet was characterized by below-average (1981–2010) melt extent and above-average surface albedo, with the net ablation being below the 2008–17 average at many test sites but still above the average for the 1961–90 reference period when the ice sheet was in steady equilibrium. Overall, total mass loss in 2017 was close to the average of the years 2003–16.

1) SURFACE MELTING

Estimates of melt extent across the GrIS are obtained from brightness temperatures measured by the Special Sensor Microwave Imager/Sounder (SSMIS) passive microwave radiometer (e.g., Mote 2007; Tedesco et al. 2013). These estimates point to a rapid start of the melting season in 2017, similar to 2016, with melt extent in early April reaching an area once typical of early June (Fig. 5.11a). From mid-June through mid-July 2017, however, melt extent was persistently below the 1981–2010 average. The spatial extent of melt for summer 2017 (June–August, JJA) was above average on 15 of 93 days (16%) and reached its maximum extent of 32.9% of the ice sheet area on 26 July. The maximum extent of surface melt in 2017 was lower than the average maximum extent of 39.8% for the period 1981–2010 and was the lowest maximum extent since 1996. There was regional variability in the characteristics of the summer melt. Most of the western and northeast ice sheet margins had more days than average with melt (relative to

1981–2010), while the southeast margin had fewer days than average. The magnitude and evolution of surface melt in 2017 were consistent with the state of the dominant atmospheric circulation pattern, as defined by the Arctic Oscillation and North Atlantic Oscillation, both of which were strongly positive (Tedesco et al. 2017).

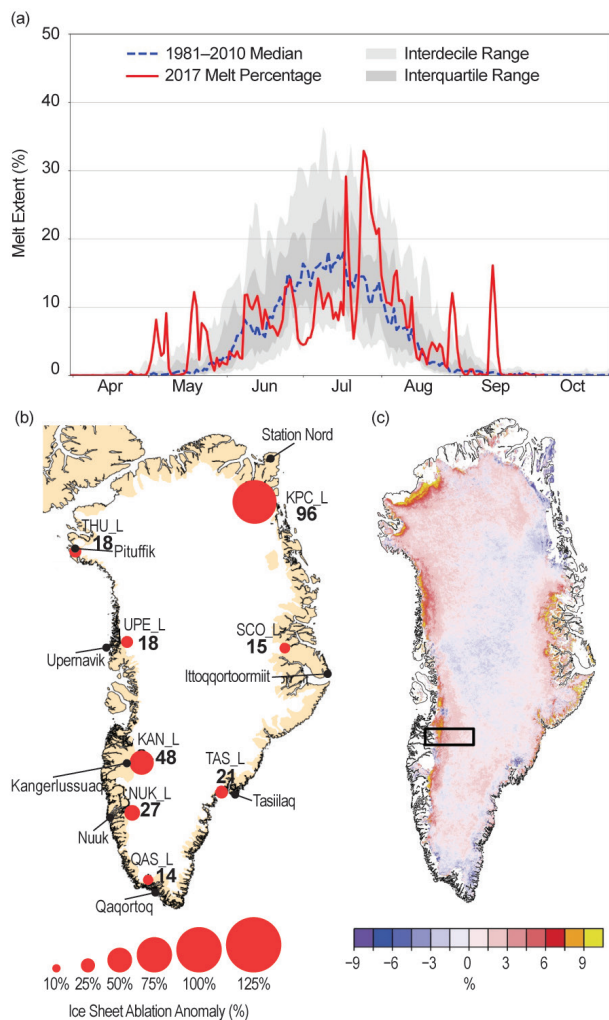


FIG. 5.11. (a) Spatial extent of melt, derived from the satellite product, as a percentage of the ice sheet area during 2017 (red line) and the 1981–2010 mean spatial extent of melt (dashed blue line). Light and dark gray areas represent the interdecile and interquartile ranges, respectively. (b) 2017 ablation anomalies (% of average, relative to 1961–90) at lower PROMICE (Programme for monitoring of the Greenland ice sheet weather station sites in the Greenland ice sheet) ablation area, using historical coastal temperature records. (c) Distribution of albedo anomalies (%; 2000–09 reference period) for summer 2017, derived from MODIS. Area within the rectangle in (c) indicates the location of the K-transect.

2) SURFACE MASS BALANCE

Consistent with the low-to-moderate surface melting described above, the August 2016–August 2017 surface mass balance (SMB) year along the K-transect at 67°N in west Greenland (Fig. 5.11b; van de Wal et al. 2012) was characterized by moderate mass loss over the ablation region (Tedesco et al. 2017). The SMB along the transect line, which has been continuously monitored for 28 years, was approximately one standard deviation below the 1990–2017 mean. The equilibrium line altitude (defined as the elevation at which mass losses balance mass gain, i.e., $SMB = 0$) in 2017 was around 1490 meters, which is 40 m below the 28-year mean. The mass balance gradient was 3.4 mm w.e. (water equivalent) $m^{-1} yr^{-1}$, which is about 6% lower than the average (Tedesco et al. 2017).

Due to the relatively low summer temperatures, net ice ablation averaged over the PROMICE sites (Fig. 5.11b), distributed around Greenland in the ablation zone, was about 20% (or 0.6 standard deviations) lower in 2017 than compared to the 2008–17 average. The largest ablation anomaly values, more than one standard deviation below average, occurred at the southwest and northwest margins. The largest absolute ablation of 5.5 m of ice was measured at the southern tip of the ice sheet. More details can be found in Tedesco et al. (2017). While the surface mass balance observations indicate that surface melt was relatively moderate in 2017, compared to that observed in the last decade, it was still higher than observed prior to 1990. When referencing the values to the 1961–90 climatological standard period (Van As et al. 2016), all eight low-elevation PROMICE station sites experienced above-average ablation anomalies in 2017 (Fig. 5.11b). However, only three stations were beyond the estimated uncertainty: KPC_L ($+96\% \pm 49\%$), SCO_L ($+15\% \pm 14\%$) and KAN_L ($+48\% \pm 35\%$).

3) ALBEDO

The area-averaged albedo (the fraction of incident solar radiation reflected by a surface) for the entire Greenland ice sheet for summer 2017 was 80.9%, as determined using data from the Moderate Resolution Imaging Spectroradiometer (MODIS; after Box et al. 2017; Fig. 5.11c). This is the third highest summer albedo value, after those of 2000 and 2013, during the 2000–17 MODIS period. Positive albedo anomalies are consistent with reduced melting in 2017 and snowfall events during the summer. The highest 2017 summer albedo anomalies occurred along the western margins of the ice sheet (Tedesco et al. 2017).

4) TOTAL MASS BALANCE

GRACE satellite gravity estimates obtained following Velicogna et al. (2014), Sasgen et al. (2012), and Luthcke et al. (2013) and available since 2002, indicate that between April 2016 and April 2017 (the most recent 12-month period of reliable data) there was a net ice mass loss of 276 ± 47 Gt (gigatonnes; Fig. 5.12). This is 144% greater than the April 2015–April 2016 mass loss (191 ± 28 Gt) and close to the average April-to-April mass loss (255 ± 7 Gt) for 2003–17 (Sasgen et al. 2012). The updated trends of total ice mass loss for the 15-year GRACE period are 264 Gt yr^{-1} (Velicogna et al. 2014) and 270 Gt yr^{-1} (Sasgen et al. 2012); the different values reflect the slightly different computational approaches adopted in the two studies. The GRACE mission came to an expected end in October 2017. No further data will be available from this important source. It is anticipated that gravity measurements from space will resume and ice mass estimates will be possible again when the GRACE follow-on mission is launched. At the time of writing, the expected launch window is in spring 2018.

5) MARINE-TERMINATING GLACIERS

Marine-terminating glaciers are the outlets by which the Greenland ice sheet discharges ice mass to the ocean. Glacier area measurements from LANDSAT and ASTER, available since 1999 (Box and Hansen 2015) for 45 of the widest and fastest-flowing marine-terminating glaciers, reveal a pattern of continued relative stability since 2012/13 (Fig. 5.13).

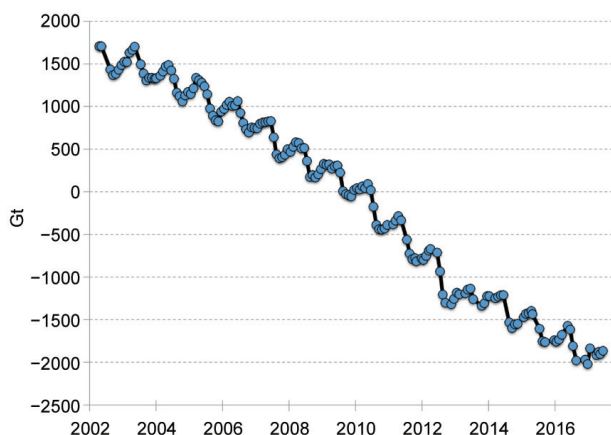


FIG. 5.12. Change in the total mass (Gt) of the Greenland ice sheet between Apr 2002 and Jun 2017, estimated from GRACE measurements. (Due to the decommissioning of the GRACE satellite, no data are available after Jun 2017.) Data are based on an unweighted average of JPL RL05, GFZ RL05, and CSR RL05 solutions, which reduce noise in the GRACE data for 2017 (Sasgen et al. 2012).

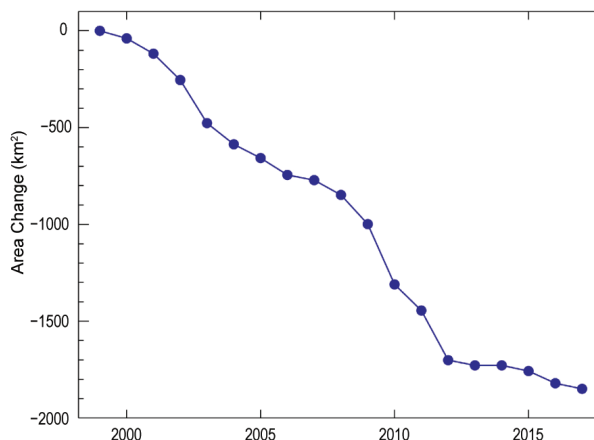


FIG. 5.13. Glacier area change (km²) from LANDSAT and ASTER imagery available since 1999 for 45 of the widest and fastest-flowing marine-terminating glaciers (after Box and Hansen 2015).

Among the surveyed glaciers, 22 retreated, 10 were stable, and 13 advanced. Overall, the annual net area change of the 45 glaciers at the end of the 2017 melt season, which started in June and ended in September, was -102.8 km². This is $\sim 80\%$ of the 18-year survey period average of -126.6 km² year⁻¹. The largest area losses were in eastern Greenland, where the Helheim and Kangerdlugssauq glaciers lost, respectively, 11.6 km² and 9.9 km² in area. The largest advance was observed at Petermann glacier, northwest Greenland, where the area increased by 11.5 km².

6) SURFACE AIR TEMPERATURES

Measurements at 20 weather stations of the Danish Meteorological Institute (Cappelen et al. 2018; Table 5.1) indicate widespread above or near-average air temperatures for 2017, relative to the period 1981–2010. The exception was during spring 2017 (March–May, MAM) in coastal northeast Greenland and the start of July in western Greenland, when many sites experienced relatively cool temperatures. Looking in more detail, during winter 2016/17 (December–February, DJF) a new seasonal record high was set in Aputiteeq, located in eastern Greenland. February in Aputiteeq was particularly warm, with a new monthly record set. At Kap Morris Jesup, along the northern coast, the winter season was the second warmest (only exceeded in 2011), with December 2016 matching the record warmth of December 2009. April 2017 was generally colder than average at many sites, compared to April 2016 when record breaking high temperatures were recorded. In autumn (September–November, SON) some individual months were record setting at Danmarkshavn, Daneborg, and Ittoqqortoormiit. At Danmarkshavn, Daneborg, and

TABLE 5.1. Seasonal and annual surface air temperature anomalies (°C) relative to the 1981–2010 average at 20 Danish Meteorological Institute weather stations in Greenland, where observations have been made for a minimum of 30 years. Seasons are winter (DJF 2016/17); spring (MAM 2017); summer (JJA 2017); autumn (SON 2017). Highlighted cell indicates a new seasonal record. The year that observations began is given, together with the station name, geographic coordinates, and elevation.

Station Name, Start Year; Latitude, Longitude, Elevation		Jan–Dec 2017	DJF 2016/17	MAM 2017	JJA 2017	SON 2017
Pituffik/Thule AFB 1948; 76.5°N, 68.8°W, 77 m a.s.l.	Anomaly (°C)	1.1	0.5	0.2	0.2	1.4
	Max Year	2010	1986	1953	1957	2010
	Min Year	1992	1949	1992	1996	1964
Upernavik 1873; 72.8°N, 56.1°W, 126 m a.s.l.	Anomaly (°C)	1.2	0.7	1.4	0.0	0.7
	Max Year	2010	1947	1932	2012	2010
	Min Year	1887	1983	1896	1873	1917
Aasiaat 1958; 68.7°N, 52.8°W, 43 m a.s.l.	Anomaly (°C)	0.9	0.8	0.6	0.3	0.8
	Max Year	2010	2010	2016	2012	2010
	Min Year	1983	1984	1993	1972	1986
Ilulissat 1807; 69.2°N, 51.1°W, 29 m a.s.l.	Anomaly (°C)	0.4	0.1	0.1	–0.5	0.5
	Max Year	2010	1929	1847	1960	2010
	Min Year	1863	1863	1813	1863	1837
Kangerlussuaq 1949; 67°N, 50.7°W, 50 m a.s.l.	Anomaly (°C)	0.6	–0.7	–0.4	0.3	0.7
	Max Year	2010	1986	2016	1960	2010
	Min Year	1984	1983	1993	1983	1982
Sisimiut 1961; 70°N, 53.7°W, 10 m a.s.l.	Anomaly (°C)	1.2	1.2	0.6	0.4	1.2
	Max Year	2010	2010	2010	2012	2010
	Min Year	1984	1984	1983	1972	1982
Nuuk 1784; 64.2°N, 51.7°W, 80 m a.s.l.	Anomaly (°C)	0.6	0.6	0.1	0.2	0.6
	Max Year	2010	2010	1932	2012	2010
	Min Year	1818	1818	1802	1819	1811
Paamiut 1958; 62°N, 49.7°W, 36 m a.s.l.	Anomaly (°C)	0.9	1.3	–0.2	0.0	1.0
	Max Year	2010	2010	2005	2010	2010
	Min Year	1984	1984	1993	1969	1982
Ivittuut/Narsarsuaq 1873; 61.2°N, 45.4°W, 27 m a.s.l.	Anomaly (°C)	1.4	1.4	1.3	0.2	0.9
	Max Year	2010	2010	2010	2016	2010
	Min Year	1884	1984	1989	1873	1874
Qaqortoq 1807; 60.7°N, 46.1°W, 32 m a.s.l.	Anomaly (°C)	0.7	1.0	0.3	–0.1	0.7
	Max Year	2010	2010	1932	1929	2010
	Min Year	1884	1863	1811	1811	1874
Kap Morris Jesup 1980; 83.7°N, 33.4°W, 4 m a.s.l.	Anomaly (°C)	1.5	5.2	0.8	0.4	–0.4
	Max Year	2011	2011	2014	1995	2016
	Min Year	1985	1988	1985	1997	1990

TABLE 5.1. (CONT.)

Station Name, Start Year; Latitude, Longitude, Elevation		Jan–Dec 2017	DJF 2016/17	MAM 2017	JJA 2017	SON 2017
Station Nord 1961; 81.6°N, 16.7°W, 36 m a.s.l.	Anomaly (°C)	1.0	2.7	–1.8	0.4	2.2
	Max Year	2016	2011	2006	2003	2016
	Min Year	1968	1967	1961	1970	1989
Danmarkshavn 1949; 76.8°N, 18.7°W, 1 m a.s.l.	Anomaly (°C)	1.1	0.6	–2.1	1.0	4.4
	Max Year	2016	2005	1976	2016	2016
	Min Year	1983	1967	1966	1955	1971
Daneborg 1958; 74.3°N, 20°W 2, 44 m a.s.l. .	Anomaly (°C)	0.5	–0.3	–3.1	0.1	4.8
	Max Year	2016	2005	1996	2016	2016
	Min Year	1968	1975	1961	1985	1971
Ittoqqortoormiit 1949; 70.5°N, 22°W, 70 m a.s.l.	Anomaly (°C)	1.0	2.5	–0.9	0.2	3.6
	Max Year	2016	2014	1996	2016	2016
	Min Year	1951	1966	1956	1955	1951
Aputiteeq 1958; 67.8°N, 32.3°W, 13 m a.s.l.	Anomaly (°C)	1.6	4.4	1.4	–0.2	2.2
	Max Year	2016	2017	1974	2016	2016
	Min Year	1973	1969	1969	1967	1973
Tasiilaq 1895; 65.6°N, 37.6°W, 53 m a.s.l.	Anomaly (°C)	1.2	2.3	1.3	0.2	1.6
	Max Year	2016	1929	1929	2016	1941
	Min Year	1899	1918	1899	1983	1917
Ikermiuarsuk 1958; 61.9°N, 42°W, 39 m a.s.l.	Anomaly (°C)	—	—	—	–0.1	1.1
	Max Year	2003	2011	1999	1961	2010
	Min Year	1983	1976	1967	1983	1969
Prins Chr. Sund 1958; 60.1°N, 42.2°W, 88 m a.s.l.	Anomaly (°C)	0.5	0.6	0.2	–0.2	1.3
	Max Year	2010	2010	2005	2010	2010
	Min Year	1993	1993	1989	1970	1982
Summit 1991; 72.6°N, 38.5°W, 3202 m a.s.l.	Anomaly (°C)	0.6	1.4	0.6	–0.6	2.7
	Max Year	2010	2010	2016	2012	2002
	Min Year	1992	1993	1992	1992	2009

Aputiteeq the autumn season was second warmest, exceeded only by 2016.

At Summit, the highest elevation of the GrIS, winter 2016/17 was the fourth warmest, with February 2017 second warmest after February 2005. May was the second warmest since 1991, after May 2010. A new July record-breaking low temperature of –33.0°C was measured at Summit on 4 July. On 28 July, a new record high July temperature of 1.9°C was measured at Summit.

f. *Glaciers and ice caps outside Greenland*—M. Sharp, B. Wouters, G. Wolken, L. M. Andreassen, D. Burgess, L. Copland, J. Kohler, S. O’Neel, M. S. Peltó, L. Thomson, and T. Thorsteinsson

The Arctic is the world’s third most heavily glaciated region, after Antarctica and Greenland. Though the total mass of glaciers and ice caps in the region is significantly less than that of the Antarctic and Greenland ice sheets, ice loss from Arctic glaciers and ice caps has become a significant contributor to current global sea level rise as a result of recent summer warming (Gardner et al. 2011, 2013; Jacob et al. 2012; Millan et al. 2017).

The state of glaciers, ice caps, and ice sheets is often described by their mass balance. The annual climatic mass balance of a glacier (B_{clim}) is defined as the difference between the annual snow accumulation on the glacier and the annual mass loss by surface melting and runoff. For the purposes of calculation, a “mass balance year” is usually taken as the period between the ends of successive summer melt seasons. Variations in the mass of most monitored Arctic glaciers and ice caps are controlled largely by changes in their climatic mass balance. However, those glaciers that terminate in the ocean [e.g., Devon Ice Cap NW (Arctic Canada), and Hansbreen and Kongsvegen (Svalbard); Table 5.2; Fig. 5.14] or in lakes can also lose mass by melting below the waterline. However, this mass balance term is rarely routinely measured.

Here, B_{clim} measurements made in 2015–16 and 2016–17 at individual glaciers monitored across the Arctic region are reported (Table 5.2; Fig. 5.14¹). All B_{clim} data are from the World Glacier Monitoring Service (WGMS 2018). Positive (negative) annual B_{clim} values indicate that a glacier gained (lost) mass over the course of the mass balance year that includes a winter accumulation season, when snow deposition typically exceeds meltwater runoff (positive mass balance), followed by a summer ablation season, when the opposite is the case (negative mass balance). The timing and duration of the accumulation and ablation seasons vary from region to region and from year to year, but in most cases, net accumulation occurs from late autumn to late spring, and net ablation from late spring to late autumn. At the time of writing, estimates for the 2016–17 mass balance year were available for only 16 glaciers [two in Alaska, nine in Iceland (nine measurement locations at seven glaciers), three in Svalbard, and two in Norway] of the 27 that are regularly monitored (Fig. 5.14). So that a complete cycle of results can be reported, B_{clim} measurements for the 2015–16 mass balance year are also reported.

Relative to the long-term (1985–2015) mean B_{clim} values, 20 of the 24 values reported for 2015–16 were more negative than the mean, and four were more positive. Five of the 18 annual net balances reported for 2016–17 were more negative than the 1985–2015 mean, and 13 were more positive. The mix of positive and negative anomalies in 2016–17 contrasts

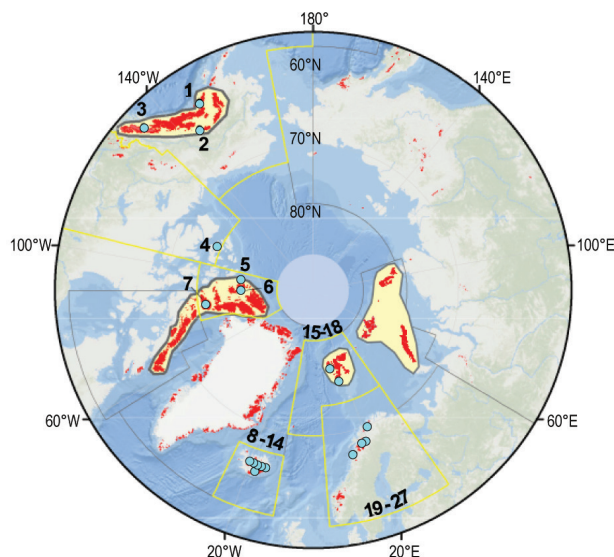


FIG. 5.14. Locations of the 27 sites on 25 Arctic glaciers and ice caps (black circles) that have long-term observations of annual climatic mass balance (B_{clim}). Areas outlined in yellow are the Randolph Glacier Inventory (RGI) regions of the Arctic (Pfeffer et al. 2014). Some individual glaciers are too close for identification and can be identified by the numbers shown at the edge of the RGI region. They can also be referenced in Table 5.2. Red shading indicates glaciers and ice caps, including ice caps in Greenland outside the ice sheet.

with the tendency for predominantly negative mass balance anomalies over the past decade. However, the long-term tendency of the cumulative B_{clim} since the mid-1990s continues to be toward more negative cumulative balances in all five regions (Fig. 5.15), indicating continuing mass loss. With the exception of Svalbard (where there has been no obvious recent acceleration of mass loss rates; Fig. 5.15), rapid mass loss across the five regions typically began during the 1990s.

New data on the length of the summer melt season at Wolverine and Gulkana glaciers in Alaska (Fig. 5.16) show that since measurements began in 1966 the summer melt season has increased by about 18 days (14%) at Wolverine Glacier, located in a maritime climate, and 24 days (24%) at Gulkana Glacier, located in a more continental climate. These data suggest that increases in summer melt played a significant role in generating more negative annual mass balances in this region.

B_{clim} measurements for the 2015–16 mass balance year are from 24 glaciers: three in Alaska, four in Arctic Canada, nine in Iceland, four in Svalbard, two in northern Norway, and two in northern Sweden (Table 5.2). All these glaciers had a negative annual B_{clim} in 2015–16. At Austre Broggerbreen and Midtre

¹ Table 5.2 lists 25 glaciers and ice caps by name while Fig. 5.14 shows the location of 27 sites where B_{clim} is measured. The difference in numbers is accounted for by Hofsjökull, Iceland, where B_{clim} is measured at three different sites on a single ice cap (no. 9 in Table 5.2).

TABLE 5.2. Measured B_{clim} climatic mass balance of 25 glaciers in Alaska (3), Arctic Canada (4), Iceland (7), Svalbard (4), and Northern Scandinavia (7) for 2015/16 and 2016/17, together with the 1985–2015 mean and standard deviation for each glacier [(Hofsjökull (Iceland) is treated as a single glacier, although measurements are made in three different sectors of this ice cap)]. (* Indicates one or more years of data missing from the record). Negative (positive) values for B_{clim} indicate mass loss (gain). Data are from the World Glacier Monitoring Service (WGMS 2018), with updates for Alaska from S. O’Neel and M. Pelto, White Glacier from L. Thomson, Svalbard from J. Kohler, and mainland Norway (Engabreen and Langfjordjokulen) from L. M. Andreassen. Numbers in column 1 refer to the glaciers located in Fig. 5.14. Results for 2016/17 may be based on measurements made before the end of the melt season and may be subject to revision.

Region	Glacier (record length, years)	B_{clim} Mean ($\text{kg m}^{-2}\text{yr}^{-1}$) (1985–2015)	B_{clim} Std. dev. ($\text{kg m}^{-2}\text{yr}^{-1}$) 1985–2015	B_{clim} ($\text{kg m}^{-2}\text{yr}^{-1}$) 2015–16	B_{clim} ($\text{kg m}^{-2}\text{yr}^{-1}$) 2016–17
Alaska					
1	Wolverine (52)	–603	1016	–400	–1160
3	Lemon Creek (65)	–640	798	–1200	–1480
2	Gulkana (52)	–778	721	–1400	—
Arctic Canada					
7	Devon Ice Cap (NW) (56)	–204	205	–483	—
5	Meighen Ice Cap (55)	–26	397	–775	—
4	Melville South Ice Cap (52)	–418	477	–792	—
6	White (54)	–308	316	–268	—
Iceland					
8	Langjökull S. Dome (19)	–1288*	855	–1677	—
9	Hofsjökull E (25)	–545*	871	–1120	–650
9	Hofsjökull N (26)	–565*	754	–830	–490
9	Hofsjökull SW (25)	–802*	1017	–450	80
10	Köldukvislarjökull (22)	–475*	738	–642	—
11	Tungnaarjökull (24)	–1128*	830	196	—
12	Dyngjujökull (18)	–146*	806	M	—
13	Brúarjökull (23)	–258*	683	–342	—
14	Eyjabakkajökull (24)	–709*	839	–930	—
Svalbard					
17	Midre Lovénbreen (49)	–379	330	–1200	–420
16	Austre Broggerbreen (50)	–486	363	–1450	–530
15	Kongsvegen (31)	–114*	360	–320	40
18	Hansbreen (28)	–397*	474	–1078	—

Lovenbreen in Svalbard, B_{clim} was the most negative ever recorded. This is attributed to relatively low snow accumulation in winter 2015–16 and high summer melt in 2016, especially in the record warm and rainy month of July. Of the 18 glaciers with measurements for both 2015–16 and 2016–17, 16 (two in Arctic Canada, all nine in Iceland, three in Svalbard, and two

in northern Scandinavia) had a more positive annual B_{clim} in 2016–17 than in the previous year, while two (both in Alaska) had a more negative annual B_{clim} than in the previous year. In Svalbard, the positive mass balance on Kongsvegen in 2016–17 is linked to above-average winter snowfall, which delayed the onset of ice melt in summer 2017.

TABLE 5.2. (CONT.)					
Region	Glacier (record length, years)	B_{clim} Mean ($\text{kg m}^{-2}\text{yr}^{-1}$) (1985–2015)	B_{clim} Std. dev. ($\text{kg m}^{-2}\text{yr}^{-1}$) 1985–2015	B_{clim} ($\text{kg m}^{-2}\text{yr}^{-1}$) 2015–16	B_{clim} ($\text{kg m}^{-2}\text{yr}^{-1}$) 2016–17
Northern Scandinavia					
19	Engabreen (48)	-127	1024	-230	-1250
20	Langfjordjokulen (27)	-948*	737	-1660	-270
21	Marmaglaciaren (24)	-460*	550	-370	—
22	Rabots Glaciar (31)	-465*	659	—	—
23	Riukojetna (26)	-592*	785	—	—
24	Storglaciaren (71)	-153	760	-240	—
25	Tarfalaglaciaren (19)	-198*	1118	—	—

Although some of the 2016–17 mass balance measurements are provisional, 12 of the reporting glaciers (two in Alaska, one in Arctic Canada, six in Iceland, two in Svalbard, and one in northern Scandinavia) had negative annual balances, and six (Meighen Ice Cap, Canada; Hofsjokull SW, Brúarjökull, and Dyngjujökull, Iceland; Kongsvegen, Svalbard; and Engabreen, Norway) had positive balances (Table 5.2).

Estimates of regional scale ice mass changes since 2011 can be derived from *CryoSat-2* radar altimetry, which measures glacier surface elevation (Wouters

et al. 2015). This approach provides regional mass change estimates for Iceland, Svalbard, the Russian Arctic, and the Canadian Arctic (Fig. 5.17). *CryoSat-2* estimates for the period 2011–17 identify the Canadian Arctic as the most important of these four regional sources of glacier mass loss (7-year mean: $-60.19 \text{ Gt yr}^{-1}$), followed by Svalbard ($-18.95 \text{ Gt yr}^{-1}$), the Russian Arctic ($-13.46 \text{ Gt yr}^{-1}$), and Iceland (-2.36 Gt yr^{-1}). Estimates for Alaska and northern Scandinavia are not available.

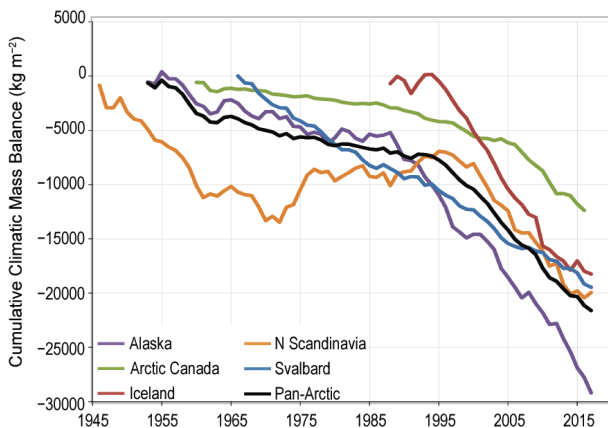


FIG. 5.15. Cumulative climatic mass balance (B_{clim} in kg m^{-2}) for glaciers and ice caps in five regions of the Arctic, and for all monitored glaciers and ice caps (Pan-Arctic). Average annual climatic balances for each region are calculated for each year using the measured annual mass balances for all monitored glaciers in the region which are then summed over the period of record to produce the cumulative B_{clim} . Note that the monitoring periods vary between regions and that the number and identity of glaciers monitored in a region may vary between years.

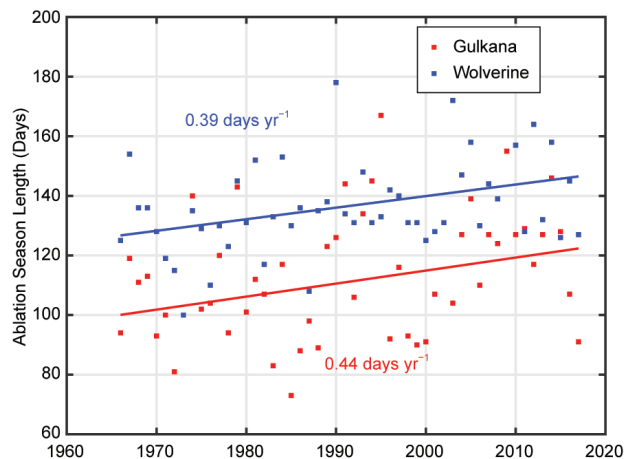


FIG. 5.16. Length (days) of the annual ablation season at Gulkana (red) and Wolverine (blue) glaciers, Alaska, showing the mean rate of change (days yr^{-1}) over the 1966–2017 observation period at each site. Coefficients of determination (r^2) determined by least squares linear regression are 0.133 for Wolverine Glacier ($p = 0.008$) and 0.08 for Gulkana Glaciers ($p = 0.04$). (Source: S. O’Neel, USGS.)

SIDEBAR 5.2: INDIGENOUS KNOWLEDGE AND THE COPRODUCTION OF KNOWLEDGE PROCESS: CREATING A HOLISTIC UNDERSTANDING OF ARCTIC CHANGE—C. BEHE AND R. DANIEL

Rapid changes occurring within the Arctic heighten the need to understand the many causes of the changes and their cumulative impacts. Most importantly, to better understand Arctic change a holistic view is needed that can only be achieved by bringing together multiple knowledge systems and scientific disciplines. This includes Arctic Indigenous Peoples and their knowledge.

Arctic Indigenous Peoples have been an integral part of the Arctic ecosystem from time immemorial and have acquired and built upon a unique knowledge system—an indigenous knowledge—shaped by that environment. It is a systematic way of thinking, which is applied to phenomena across biological, physical, cultural, and spiritual systems. It includes insights based on evidence acquired through direct and long-term experiences and extensive and multigenerational observations, lessons, and skills.

Indigenous knowledge has developed over millennia and is still developing in a living process, including knowledge acquired today and in the future, and it is passed on from generation to generation (Inuit Circumpolar Council-Alaska 2016). Indigenous knowledge stresses the importance of understanding interconnecting systems, that is, ecological, physical, cultural, and social systems, the relationship between those components, and the need to understand cumulative impacts (Inuit Circumpolar Council-Alaska 2015). This world view and way of understanding will aid in gaining a holistic understanding of the Arctic and the changes that are occurring there.

To gain a truly holistic understanding of the changing Arctic, it is necessary to bring together indigenous knowledge and science through a coproduction of knowledge process. Such a process offers opportunities to bring together different knowledge systems to develop adaptation policies and practices for sustainability, and to address biodiversity conservation and ecosystem-based management in a changing Arctic.

The coproduction of knowledge process brings together indigenous knowledge holders and scientists to work in partnership from the inception of a project, for example, identification of research questions and hypotheses, through analysis and output. Equity is a cornerstone of the process, ensuring fairness and the opportunity to engage in all aspects of a project. All participants have a fair and equal chance of succeeding. The coproduction of knowledge process requires culturally appropriate

methodologies in data collection and analyses to be agreed upon by all knowledge holders.

Successful coproduction of knowledge fosters an environment of trust and respect, works toward empowerment and capacity building, and recognizes indigenous knowledge sovereignty; it is important to recognize the sovereign rights of indigenous peoples, including those related to their own knowledge. This includes indigenous peoples fully understanding the risks and opportunities of participating in a research project, having authority over how data and information are shared, and the right to not participate in a research project. The principles of free, prior, and informed consent are critical to the coproduction of knowledge process (UN General Assembly 2007).

Successful coproduction of knowledge is built upon long-term partnerships. A good first step is an understanding of the lay of the land in indigenous homelands. Just as scientists understand the importance of networks in their research, so indigenous peoples also live in complex social and governance systems, allowing the opportunity to leverage existing indigenous networks, institutions, and organizations. It is important to understand partnership building from an indigenous perspective and to know that partnership and participation are not synonymous. Clear, transparent, culturally appropriate terms of reference are recommended to ensure there are no misunderstandings and to help with relationship building.

Indigenous knowledge and modern science have different approaches, methodologies, analyses, and validation processes. The coproduction of knowledge process requires respect for each knowledge system and avoiding translation of one knowledge system into the other, that is, trusting an indigenous knowledge holder's ability to analyze their own information and respect that each person at the table comes with the credentials needed to be there. While some credentials are built from academic degrees and publications, others come from holding and demonstrating a body of knowledge through a lifetime of hunting, fishing, gathering, or being an elder.

Many Arctic science projects have aimed to build partnerships with indigenous communities, but few have used a true coproduction of knowledge process that brings together indigenous knowledge holders and scientists equitably from the inception of the project. An exemplar that demonstrates the process is the Ikaaġvik

Sikukuun (Ice Bridges) project in Kotzebue in northwest Alaska (Mahoney et al. 2017). This four-year (2017–20) project, which aims to understand fundamental processes underlying the mechanisms and impacts of changing coastal sea ice, first brought together indigenous knowledge holders with scientists from different disciplines to develop the research focus and questions, decide on a methodology, and then agree on a plan for implementing the project together. Indigenous knowledge will also inform the synthesis and dissemination of the results of the project.

The success of a coproduction of knowledge process must be defined by both the indigenous knowledge holders and scientists involved in a project. Experts from both knowledge systems must agree that a coproduction of knowledge occurred and it will hold all of the basic elements presented here. These include recognizing and working toward equity through building capacity, empowering indigenous partners, fostering an environment for trust and respect, building a collaborative process that involves multiple steps and continuous evaluation and which is defined by all those involved in a project, and respecting indigenous knowledge sovereignty.

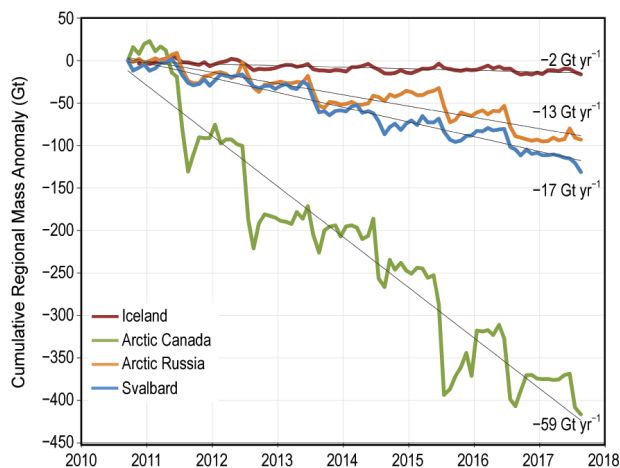


FIG. 5.17. Cumulative regional glacier mass anomalies (in, Gt) for Iceland, Arctic Canada, Arctic Russia, and Svalbard, derived using data from CryoSat2 radar altimetry (2011–17) (B. Wouters, Utrecht University). Cumulative mass anomalies in each region are defined relative to the glacier mass measured in the region at the start of the measurement period. Trend lines and average annual rates of mass change (Gt yr^{-1}) in each region are shown. Annual cycles in the accumulation and removal of mass are evident in each region.

g. *Terrestrial permafrost*—V. E. Romanovsky, S. L. Smith, K. Isaksen, N. I. Shiklomanov, D. A. Streletskiy, A. L. Kholodov, H. H. Christiansen, D. S. Drozdov, G. V. Malkova, and S. S. Marchenko

Permafrost is an important component of the Arctic landscape, influencing hydrological systems and ecosystems, and presenting challenges for built infrastructure, for example, buildings, roads, railways, airports, and pipelines. Permafrost temperature and active layer thickness (ALT) are key indicators of changes in permafrost conditions. Permafrost is defined as earth materials (e.g., soil, rock) that exist at or below 0°C continuously for at least two consecutive

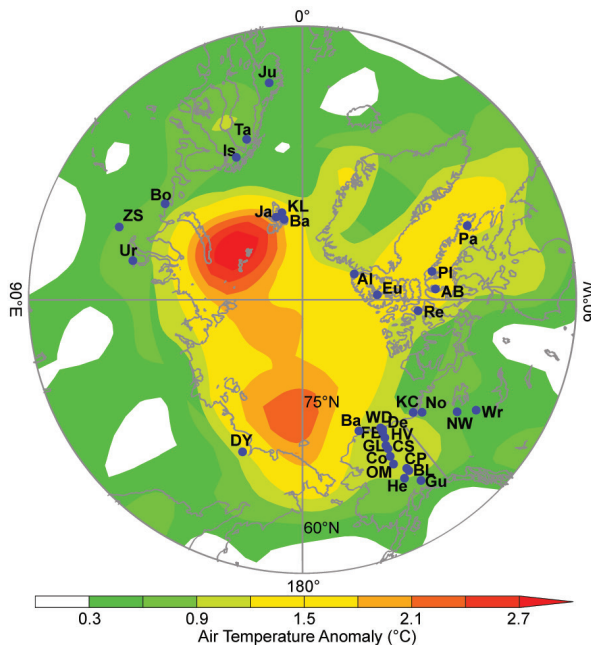


FIG. 5.18. Location of the permafrost temperature monitoring sites shown in Fig. 5.19 superimposed on average surface air temperature anomalies ($^{\circ}\text{C}$) during 2000–16 (with respect to the 1981–2010 mean) from the NCEP-reanalysis (Kalnay et al. 1996). Data provided by the NOAA/ESRL Physical Sciences Division (www.esrl.noaa.gov/psd/). Sites shown in Fig. 5.19 for (a) Barrow (Ba), West Dock (WD), KC-07 (KC), Duvany Yar (DY), Deadhorse (De), Franklin Bluffs (FB), Galbraith Lake (GL), Happy Valley (HV), Norris Ck (No); (b) College Peat (CP), Old Man (OM), Chandalar Shelf (CS), Birch Lake (BL), Coldfoot (Co), Norman Wells (NW), Wrigley 1 and 2 (Wr), Healy (He), Gulkana (Gu); (c) Eureka EUK4 (Eu), Alert BH1, BH2, and BH5 (Al), Rolute (Re), Arctic Bay (AB), Pond Inlet (PI), Pangnirtung (Pa); (d) Janssonhaugen (Ja), Bay-elva (Ba), Kapp Linne 1 (KL), Urengoy #15-06 and #15-10 (Ur), Juvvasshøe (Ju), Tarfalaryggen (Ta), Polar Urul (ZS), Bolvansky #56, #59, and #65 (Bo), Iskoras Is-B-2 (Is). Information about these sites is available at <http://gtnpdatabase.org/>, http://perma-frost.gi.alaska.edu/sites_map, and www2.gwu.edu/~calm/data/data-links.html.

years. The active layer is the seasonally thawed layer above the permafrost. Permafrost temperatures, at a depth where seasonal temperature variations are negligible, are powerful indicators of long-term change. On the other hand, the active layer responds to shorter term fluctuations in climate and is especially sensitive to changes in summer air temperature and precipitation. Warming and thawing of permafrost in the Arctic are reported here.

Changes up to 2017 (most recent data available) in mean annual permafrost temperatures and ALT are summarized for a number of sites throughout the Arctic (Fig. 5.18). Recent long-term changes in permafrost temperature are driven mostly by air temperature trends (Romanovsky et al. 2015). Other important influences on permafrost temperature, such as snow depth and density, vegetation characteristics, and soil moisture, can affect the observed permafrost temperature trends at the local scale. In general, the increase in permafrost temperatures observed since the 1980s is more significant in the higher latitudes where the largest increase in air temperature is observed (Fig. 5.18).

I) PERMAFROST TEMPERATURES

Temperatures in the cold continuous permafrost of northern Alaska, Northwest Territories (Canada), and northeastern East Siberia continue to rise (Fig. 5.19a). In 2017 on the North Slope of Alaska, record high temperatures at 20-m depth occurred at all permafrost observatories (Barrow, West Dock, Franklin Bluffs, Happy Valley, and Deadhorse; Fig. 5.19a) with the exception of Galbraith Lake. The permafrost temperature increase (+0.1° to +0.2°C) between 2016 and

2017 was substantial and comparable to the highest rate of warming observed in this region, which occurred during 1995–2000 (Fig. 5.19a). Since 2000, permafrost temperature increase at 20-m depth in this region has ranged from 0.21° to 0.66°C decade⁻¹ (Fig. 5.19a; Table 5.3).

In Interior Alaska, following the slight cooling of 2007–13, permafrost temperatures increased and were higher in 2017 than in 2016 at all sites (Coldfoot, Old Man, College Peat, Birch Lake, Gulkana, and Healy in Fig. 5.19b). The largest changes, at Birch Lake and Old Man, were associated with new record highs in 2017 for the entire 33-year measurement period (Fig. 5.19b; Table 5.3).

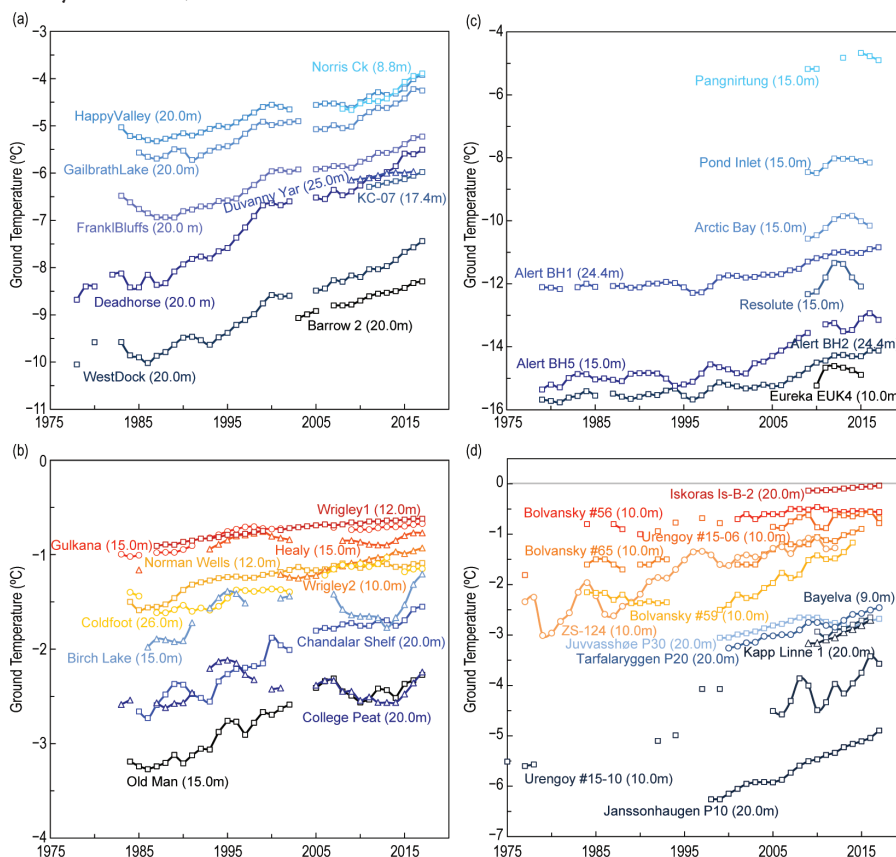


FIG. 5.19. Time series of mean annual ground temperature (°C) at depths of 9 to 26 m below the surface at selected measurement sites that fall roughly into priority regions of the Adaptation Actions for a Changing Arctic Project (AMAP 2015): (a) cold continuous permafrost of northern Alaska, Northwest Territories (Canada), and NE East Siberia; (b) discontinuous permafrost in Interior Alaska and northwestern Canada; (c) cold continuous permafrost of eastern and High Arctic Canada (Baffin Davis Strait); and (d) continuous to discontinuous permafrost in Scandinavia, Svalbard, and Russia/Siberia (Barents region). Temperatures are measured at or near the depth of zero annual amplitude where the seasonal variations of ground temperature are negligible. Note that the temperature scales are different in each graph. Data are updated from Christiansen et al. 2010; Romanovsky et al. 2017; Smith et al. 2015, 2017; Ednie and Smith 2015; Boike et al. 2018.

TABLE 5.3. Change in mean annual ground temperature ($^{\circ}\text{C decade}^{-1}$) for sites shown in Fig. 5.19. For sites where measurements began prior to 2000, the rate for the entire available record is provided as well as the rate for the period after 2000. The names of the stations with record high temperatures in 2017 are shown in red. Note that some records only began after 2007, as shown in Fig. 5.19.

Region	Sites	Entire Record	Since 2000
Alaskan Arctic plain	West Dock (WD), Deadhorse (De), Franklin Bluffs (FB), Barrow (Ba)	+0.36 to +0.8	+0.44 to +0.65
Northern foothills of the Brooks Range, Alaska	Happy Valley (HV), Galbraith Lake (GL)	+0.3 to +0.42	+0.34 to +0.47
Southern foothills of the Brooks Range, Alaska	Coldfoot (Co), Chandalar Shelf (CS), Old Man (OM)	+0.08 to +0.35	+0.14 to +0.25
Interior Alaska	College Peat (CP), Birch Lake (BL), Gulkana (Gu), Healy (He)	+0.07 to +0.22	+0.03 to +0.1
Central Mackenzie Valley	Norman Wells (NW), Wrigley (Wr)	Up to +0.1	<+0.1 to +0.2
Northern Mackenzie Valley	Norris Ck (No), KC-07(KC)	—	+0.5 to +0.9
Baffin Island	Pangnirtung (Pa), Pond Inlet (PI), Arctic Bay (AB)	—	+0.5 to +0.7
High Canadian Arctic	Resolute (Re), Eureka (Eu)	—	+0.4 to +0.7
High Canadian Arctic	Alert (Al) at 15 m 24m	+0.5 +0.3 to +0.4	+1.2 +0.7 to +0.9
North of East Siberia	Duvany Yar (DY)	—	+0.3
North of West Siberia	Urengoy 15-06 and 15-10 (Ur)	+0.31 to +0.47	+0.1 to +0.19
Russian European North	Bolvansky 56, 59, and 65 (Bo), Polar Ural (ZS-124)	+0.18 to +0.46	+0.1 to +0.83
Svalbard	Janssonhaugen (Ja), Bayelva (Ba), Kapp Linne I (KL)	+0.7	+0.6 to +0.7
Northern Scandinavia	Tarfalarggen (Ta), Iskoras Is-B-2 (Is)	—	+0.1 to +0.4
Southern Norway	Juvvasshøe (Ju)	+0.2	+0.2

In northwestern Canada, the temperature of permafrost in the central Mackenzie Valley (Norman Wells and Wrigley in Fig. 5.19b; Table 5.3) has generally increased since the mid-1980s (Smith et al. 2017). Although less warming has been observed since 2000, permafrost temperatures in 2017 at these sites were the highest recorded. Greater recent warming has been observed in the colder permafrost of the northern Mackenzie region (Norris Ck, KC-07 in Fig. 5.19a and Table 5.3; Smith et al. 2017), with the highest temperatures during the observation period occurring in 2016/17.

In northeastern Canada, the 2016/17 mean permafrost temperatures in the upper 25 m of the ground at Alert, northernmost Ellesmere Island in the high Arctic, were among the highest recorded since 1978 (Fig. 5.19c). Although permafrost at Alert has generally warmed since 1978, permafrost temperatures have increased at a higher rate since 2000 (Table 5.3; Smith et al. 2015), consistent with air temperature trends (Fig. 5.18). There has been little change at Alert since 2010 (Fig. 5.19c), which coincides with a period of lower mean annual air temperatures. At other sites in the Queen Elizabeth Islands (Resolute and Eureka) and on Baffin Island (Pangnirtung, Pond Inlet, and

Arctic Bay), permafrost temperature measurements since 2008, at 10- to 15-m depth, indicate an overall warming (Fig. 5.19c; Table 5.3). A decrease in permafrost temperature since 2012 appears to be associated with lower mean annual air temperatures over the last few years in the region.

Increases in permafrost temperature over the last 30–35 years in northern Russia have been similar to those in northern Alaska and the Canadian high Arctic (Drozdov et al. 2015). In the Russian European North and western Siberian Arctic, temperatures at 10-m depth have increased by ~0.4° to 0.6°C decade⁻¹ since the late 1980s at colder permafrost sites (Fig. 5.19d, sites Bolvansky #59, Urengoy #15-06 and #15-10) and increased less in warmer permafrost sites (Table 5.3; Fig. 5.19d, sites Bolvansky #56 and Urengoy #15-06; Drozdov et al. 2015). In these regions, there are differences in permafrost temperature (cold vs. warm) because surface conditions such as vegetation, surface wetness, and soil moisture vary according to landscape types, while climatic conditions are largely independent of surface condition and landscape.

In the Nordic region, where the temperature at 20-m depth has increased between 0.1° and 0.7°C decade⁻¹ (Fig. 5.19d; Table 5.3) since 2000, warming and thawing of permafrost have been observed recently (Christiansen et al. 2010; Isaksen et al. 2011; Farbrot et al. 2013). Lower rates of warming occur where permafrost temperatures are close to 0°C and latent heat effects related to melting ground ice

are important. Greater warming occurred in colder permafrost on Svalbard and in northern Scandinavia (Table 5.3). In the discontinuous permafrost zone of southern Norway, permafrost warmed between 2015 and 2017, following a period of cooling between 2011 and 2014 (Fig. 5.19d).

2) ACTIVE LAYER THICKNESS

In 2017, standardized, mechanical probing of ALT was conducted at 76 Circumpolar Active-Layer Monitoring (CALM) program sites in Alaska and Russia. Each site consists of a spatial grid varying from 1 ha to 1 km² in size and is representative of the regional landscape (Shiklomanov et al. 2012). Additional active-layer observations, derived from thaw tubes (Duchesne et al. 2015), are available from 25 Canadian sites located in the Mackenzie Valley, northwestern Canada.

The average ALT in 2017 for 20 North Slope of Alaska sites was 0.52 m, which is 0.06 m (or +12%) higher than the 1996–2005 mean and is one of the highest in the 22-year data record. Previous maxima occurred in 1998, 2013, and 2016 (Fig. 5.20). The interior of Alaska is characterized by a pronounced ALT increase over the last 22 years (Fig. 5.20). However, after reaching the 22-year maximum of 0.77 m in 2016, the 2017 ALT decreased by 10% to 0.69 m.

Records from the sites with thaw tubes in the Mackenzie Valley indicate that there has been a general increase in ALT in this region since 2008 (Fig.

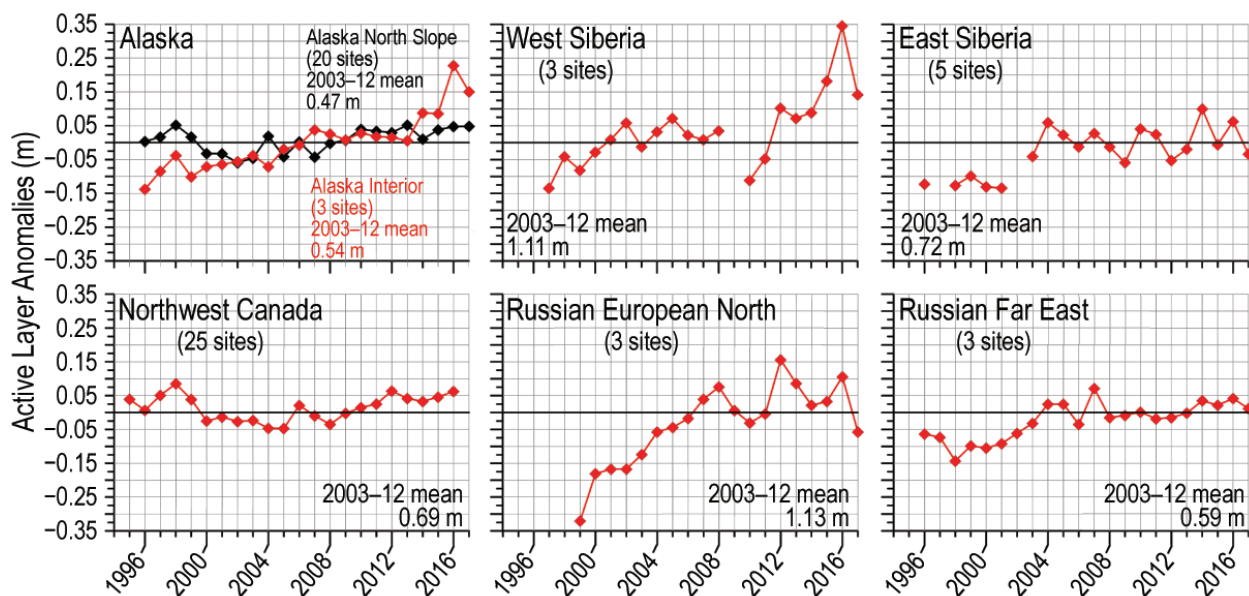


FIG. 5.20. Long-term annual active-layer thickness change (m) in six different Arctic regions for 2017 as observed by the CALM program relative to the 2003–12 mean. Positive (negative) anomaly values indicate the active layer was thicker (thinner) than average. Thaw depth observations from the end of the thawing season were used. Only sites with at least 20 years of continuous thaw depth observations are shown.

5.20; Duchesne et al. 2015; Smith et al. 2017). ALT in 2016 (most recently available data) was on average 0.06 m greater than the 2003–12 mean, similar to the previous peak value in 2012.

A decrease in ALT from 2016 to 2017 was reported for all Russian regions. In West Siberia, the average 2017 ALT was 1.25 m, which is 0.2 m (or 14%) smaller than the 20-year maximum observed in 2016. In the Russian European North, the 2017 ALT was 1.08 m compared to 1.24 m in 2016. A 2017 ALT of 0.69 m was reported for East Siberia, which is 0.1 m smaller than the regional average 2016 ALT value. The smallest decrease was reported in the Russian Far East (Chukotka), where the ALT in 2017 was 0.03 m (or 5%) less than that reported in 2016.

In the Nordic region, active layer records (1999–2017) indicate a general ALT increase of 0.10 to 0.30 m since 1999. The particularly warm summer of 2014 in the Nordic region contributed to the thickest active layer measured so far at some places.

h. Tundra greenness—H. Epstein, U. Bhatt, M. Reynolds, D. Walker, J. Pinzon, C. J. Tucker, B. C. Forbes, T. Horstkotte, M. Macias-Fauria, A. Martin, G. Phoenix, J. Bjerke, H. Tømmervik, P. Fauchald, H. Vickers, R. Myneni, T. Park, and C. Dickerson

Vegetation in the Arctic tundra has been responding to environmental changes over the course of the last several decades, with the tendency being an increase in the amount of above-ground vegetation, that is, “greening” (Bhatt et al. 2010). These vegetation changes vary spatially throughout the circumpolar Arctic in both direction and magnitude, and they are not always consistent over time. This suggests complex interactions among the atmosphere, ground (soils and permafrost), vegetation, and animals of the Arctic system. Changes in tundra vegetation can have important effects on permafrost, hydrology, carbon and nutrient cycling, and the surface energy balance (e.g., Frost et al. 2017; Keęski et al. 2017), as well as the diversity, abundance, and distribution of both wild and domesticated herbivores (e.g., Fauchald et al. 2017; Horstkotte et al. 2017). We continue to evaluate the state of the circumpolar Arctic vegetation, to improve our understanding of these complex interactions and their impacts on the Arctic system and beyond.

The reported controls on tundra greening are numerous and varied. They include increases in summer, spring, and winter temperatures and increases in growing season length (Bhatt et al. 2017; Fauchald et al. 2017; Horstkotte et al. 2017; Myers-Smith et al. 2018; Vickers et al. 2016), in part controlled by reductions in Arctic Ocean sea ice cover (Bhatt et al.

2017; Macias-Fauria et al. 2017; see Section 5d). Other controls on tundra greening include increases in snow water equivalent (see Section 5i) and soil moisture, increases in active layer depth (see Section 5g), changes in the patterns of herbivore activity, and even a reduction in the human use of the land (Fauchald et al. 2017; Horstkotte et al. 2017; Martin et al. 2017; Westergaard-Nielsen et al. 2017).

Using Earth-observing satellites with subdaily return intervals, Arctic tundra vegetation has been continuously monitored since 1982. Here, data are reported from the Global Inventory Modeling and Mapping Studies (GIMMS) 3g V1 dataset, based largely on the AVHRR sensors aboard NOAA satellites (Pinzon and Tucker 2014). At the time of writing, the GIMMS3g V1 dataset was only available through 2016. The GIMMS product (at 1/12° resolution for this report) is a biweekly, maximum-value composited dataset of the normalized difference vegetation index (NDVI). NDVI is highly correlated with above-ground vegetation (e.g., Reynolds et al. 2012), or “greenness,” of the Arctic tundra. Two metrics based on the NDVI are used: MaxNDVI and TI-NDVI. MaxNDVI is the peak NDVI for the year (growing season) and is related to yearly maximum above-ground vegetation biomass. TI (time-integrated) NDVI is the sum of the biweekly NDVI values for the growing season and is correlated with the total above-ground vegetation productivity.

Examining the overall trend in tundra greenness for the now 35-year record (1982–2016), it is apparent that the MaxNDVI and the TI-NDVI have increased throughout most of the circumpolar Arctic tundra (Fig. 5.21). Regions with some of the greatest increases in tundra greenness are the North Slope of Alaska, the low Arctic (southern tundra subzones) of the Canadian tundra, and eastern Siberia. However, tundra greenness has declined (i.e., the tundra has been “browning”) on the Yukon–Kuskokwim Delta of western Alaska, in the high Arctic of the Canadian Archipelago, and in northwestern Siberia. Regions of greening and browning, measured by NDVI increases and decreases, respectively, tend to be consistent between MaxNDVI and TI-NDVI.

Following 2–3 years of successive declines prior to and including 2014, the NDVI or greenness of Arctic tundra increased in 2015 and 2016 for both indices (MaxNDVI and TI-NDVI) and both continents (North America and Eurasia), exhibiting substantial recovery from the previous years of “browning.” (Fig. 5.22). One exception was the TI-NDVI for North America, which continued to decrease in 2015. MaxNDVI and TI-NDVI for the entire Arctic

increased 6.0% and 9.3%, respectively, between 2015 and 2016. MaxNDVI in North America increased by 6.3% compared to 5.4% in Eurasia. The first substantial annual increase in TI-NDVI for North America since 2010 occurred in 2016, potentially due to the high growing season temperatures that year.

All NDVI values for 2016 were greater than their respective mean values for the 35-year record. MaxNDVI values ranked second, third, and first for the Arctic, Eurasian Arctic, and North American Arctic, respectively. TI-NDVI values ranked first, first, and second for the Arctic, Eurasian Arctic,

and North American Arctic, respectively. Based on remotely-sensed land surface temperatures (LST) from the same sensors as those providing the NDVI values, the summer warmth index (SWI: sum of mean monthly temperatures >0°C) for the Arctic as a whole and for the Eurasian Arctic was greater in 2016 than in any other year of the satellite record (since 1982). For the North American Arctic, the 2016 SWI was the second highest on record (very close to the highest value in 1994).

Even though the past two years have seen large increases in tundra NDVI, there are still regions of the Arctic that have experienced browning over the length of the satellite record. There have also been substantial periods of tundra browning even within a general greening trend. While research on tundra browning is still relatively sparse, there has recently been greater attention given to this phenomenon. Bjerke et al. (2017) report on extensive vegetation dieback in northern Norway (including Svalbard) in 2014 and 2015. They attributed this dieback largely to

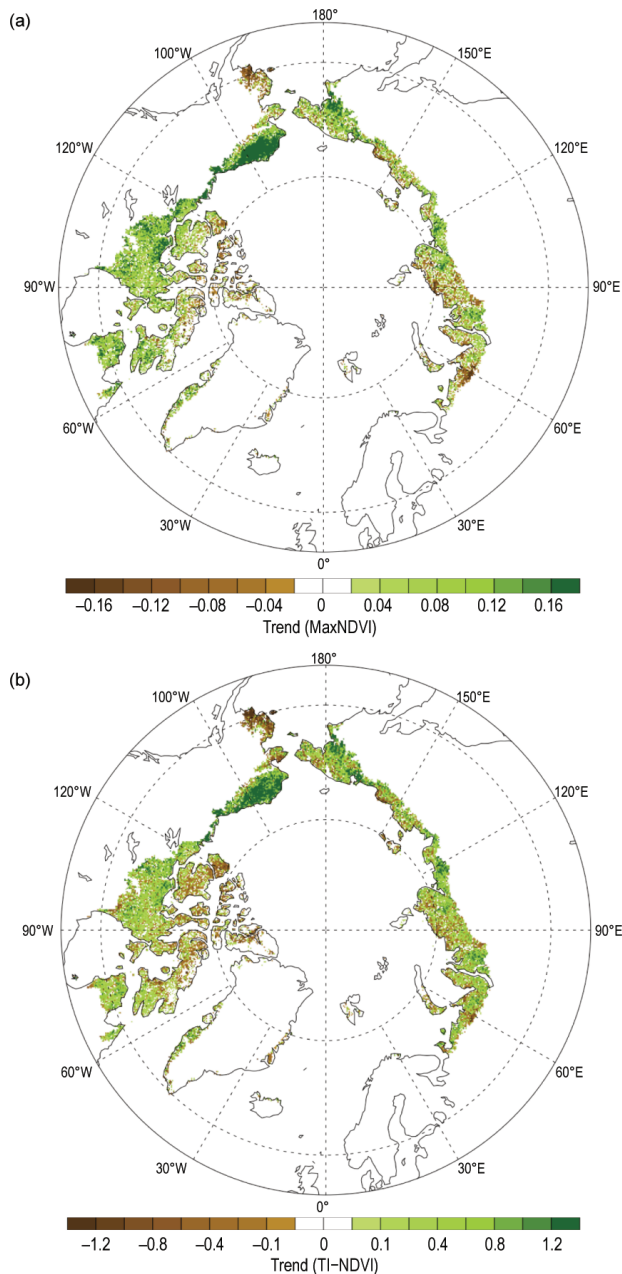


FIG. 5.21. (a) Magnitude of the trend in (a) MaxNDVI and (b) TI-NDVI for 1982–2016

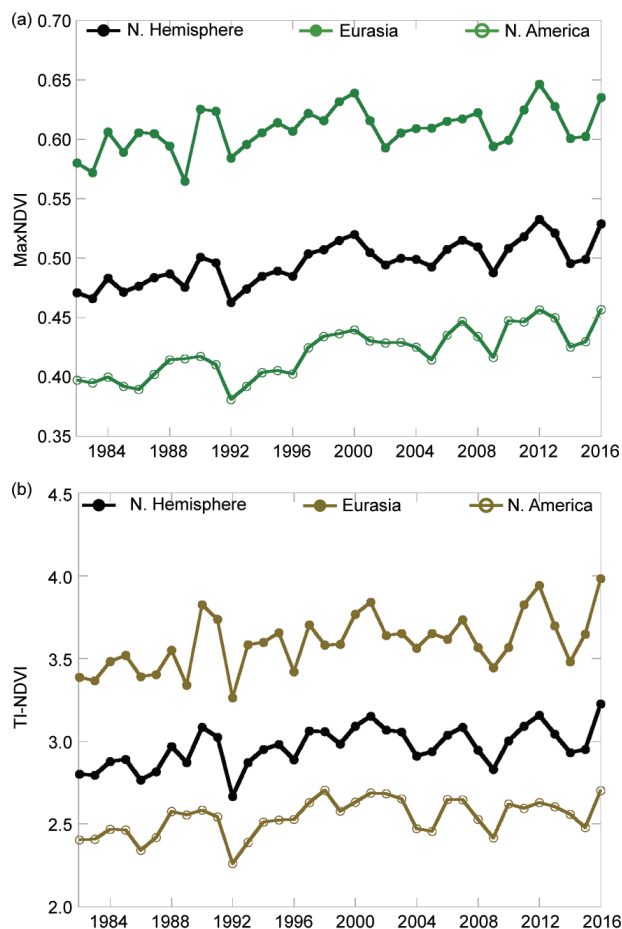


FIG. 5.22. (a) MaxNDVI and (b) TI-NDVI for Eurasia (top), the Arctic as a whole (middle), and North America (bottom) for 1982–2016.

SIDEBAR 5.3: WILDLAND FIRE IN BOREAL AND ARCTIC NORTH AMERICA—A. YORK, U. BHATT, R. THOMAN, AND R. ZIEL

Despite the low temperatures and short growing seasons of northern ecosystems, wildland fire is the dominant ecological disturbance in the boreal forest, the world's largest terrestrial biome. Wildland fire also affects adjacent tundra regions. This sidebar, with a focus on the 2017 Alaska fire season, addresses the history and variability of fire disturbance in Alaska (US) and Northwest Territories (Canada), outlines how short-term weather conditions (temperature, precipitation, convection, and wind) influence area burned, and discusses projections for future tendencies in fire susceptibility.

Beyond immediate threats to lives and property, fire impacts include compromised human health and limited visibility due to smoke. Fire disturbance affects terrestrial ecosystems at multiple scales, including carbon release through combustion (Kasischke et al. 2000). About 35% of global soil carbon is stored in tundra and boreal ecosystems (Scharlemann et al. 2014) that are potentially vulnerable to fire disturbance (Turetsky et al. 2015). Other impacts include interactions with vegetation succession (Mann et al. 2012; Johnstone et al. 2010), biogeochemical cycles (Bond-Lamberty et al. 2007), energy balance (Rogers et al. 2015), and hydrology (He, Liu et al. 2005). Combustion of the insulating surface organic layer can destabilize underlying permafrost. Because permafrost impedes drainage and ice-rich permafrost settles upon thawing (thermokarst), accelerating degradation of the permafrost may have large consequences for northern ecosystems (Jorgenson et al. 2010; Jones et al. 2015).

Weather is a dominant control of fire activity on a year-to-year basis. Over the longer term, high-latitude fire regimes appear to be responding rapidly to environmental changes associated with the warming climate. Although highly variable, area burned has increased since the 1960s in much of boreal North America (Kasischke and Turetsky 2006; Gillett et al. 2004). Over that time, both the number and size of individual fire events has increased, contributing to more frequent large fire years in northwestern North America (Ka-

sischke and Turetsky 2006). Figure SB5.3 shows area burned each year since 1980 in Alaska and Northwest Territories, including both boreal and tundra regions.

Although highly variable, high-latitude fire seasons generally begin and end earlier than in more temperate areas

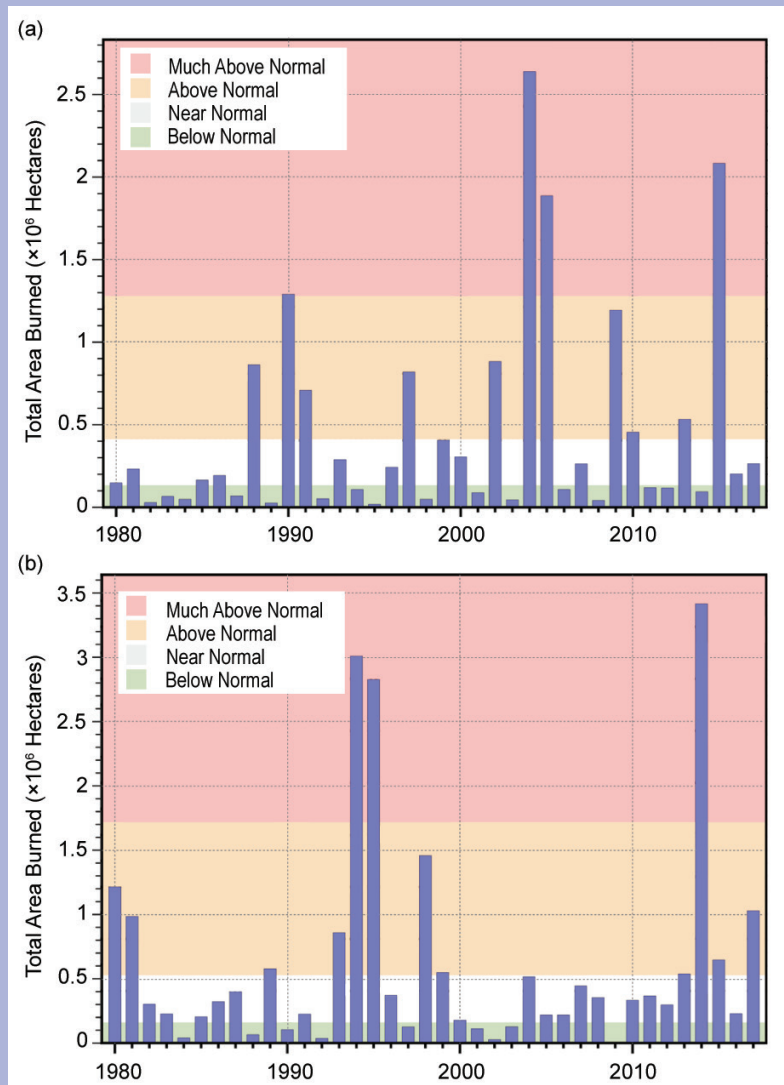


FIG. SB5.3. Annual area burned (ha) each year since 1980 in (a) Alaska and (b) Northwest Territories (Canada), including both boreal and tundra regions. Note that high fire years are not coincident in these subregions, indicating the importance of local weather and other conditions (e.g., fuels, ignition). Category definitions used here are from the fitted log-normal distribution to the observed 1980–2017 area burned; below normal is the 0–33rd percentiles, near normal is the 33rd–66th percentiles, above normal is the 66th–90th percentiles, much above is greater than the 90th percentile.

(Fig. SB5.4). Depending on weather, fire danger can increase as soon as areas are snow-free in April and May; season-ending rains typically fall in July or August, but their absence can extend the season into September, as in the record years of 2004 (2.67 million ha) and 2005 (1.88 million ha) in Alaska. Recent large fire seasons in high latitudes include 2014 in Northwest Territories (Fig. SB5.3), where 385 fires burned 3.4 million ha, and 2015 in Alaska (Fig. SB5.3), where 766 fires burned 2 million ha—the latter was more than half the total area burned in the entire United States (NWT 2015; AICC 2015). Northern communities threatened or damaged by recent wildfires include Fort McMurray, located in the boreal forest in Alberta, Canada, where 88000 people were evacuated and 2400 structures were destroyed in May 2016 (Kochtubajda et al. 2017). The 2007 Anaktuvuk River Fire is the largest (104000 ha) and longest-burning (almost 3 months) fire known to have occurred on the North Slope of Alaska and initiated widespread thermokarst development (Jones et al. 2015).

Most area burned in northern ecosystems occurs during sporadic periods of high fire activity. Half of the area burned in Alaska from 2002 to 2010 was consumed over just 36 days (Barrett et al. 2016). Recent analyses have identified a temperature threshold in Alaska with a much greater likelihood of fire occurrence within a 30-year period at locations where mean July temperatures exceed 13.4°C (Young et al. 2017). Large fire events require the confluence of warm and dry weather conditions with a source of ignition (often lightning from convective thunderstorms) and fuels that can carry fire. High latitude ecosystems are characterized by unique fuels, in particular, fast-drying beds of mosses, lichens, and accumulated organic material (duff) that underlie resinous shrubs and dense, highly flammable conifers. These understory fuels dry rapidly during periods of warm, dry weather and the long day lengths of June and July. Consequently, extended drought is not required to increase fire danger to extreme levels.

Historically, lightning is responsible for the majority of the acreage burned in high latitudes, as lightning-ignited fires occur in more remote locations and thus are subject to lower levels of suppression than human-started incidents. Veraverbeke et al. (2017) showed that lightning ignitions have increased in boreal

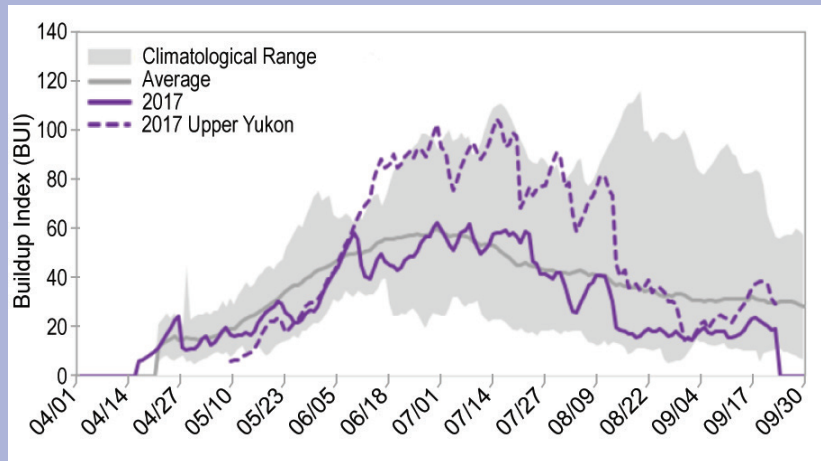


FIG. SB5.4. Average (gray line) and climatological range (gray shading) of BUI between 1 Apr and 30 Sep in Alaska's boreal interior for 1994–2017, compared to the 2017 average (solid purple line) and the 2017 predictive service area AK02 (Upper Yukon and surrounding uplands, centered around the Arctic Circle; dashed purple line). While the boreal interior average BUI for 2017 (purple line) was similar to the historic average BUI (gray line), the Upper Yukon Zone (dashed purple line), where the majority of the hectares burned in the territory in 2017, showed a significant elevation in BUI from mid-Jun to mid-Aug.

North America since 1975 and were a major contributor in the extreme 2014 Northwest Territories and 2015 Alaska fire seasons. In addition, Partain et al. (2016) found that human-induced climate change—manifested as a combination of high surface air temperatures, low relative humidity, and low precipitation—increased the likelihood of the extremely dry fuel conditions seen in Alaska in 2015 by 34%–60%.

The snow-free season has increased by approximately 5 days decade⁻¹ in Alaska since 1979 (Liston and Hiemstra 2011). In response, in 2006 Alaska's fire management agencies shifted the statutory start of fire season ahead by a month, from 1 May to 1 April, to better prepare for early season events. In addition to adapting to long-term trends, managers in Alaska and Canada must track day-to-day variability in threats to dispersed populations with limited resources. Managers in both regions use the Canadian fire weather index (FWI) system on a daily basis to estimate the spatial and temporal distribution of wildfire potential from observed and forecast weather conditions (Lawson and Armitage 2008). Among the FWI indices, the buildup index (BUI), based on cumulative scoring of daily temperature, relative humidity, and precipitation, represents seasonal variability in fuel availability and flammability (Fig. SB5.4). A BUI threshold of 80 has been identified as a critical indicator of fire growth potential in Alaska (Ziel et al. 2015).

In 2017, the typical area burned in Alaska (264 221 ha; Fig. SB5.3) was reflected in a fairly normal BUI across the boreal region that essentially paralleled the climatological average (Fig. SB5.4). However, the impact of a “normal” season can fall disproportionately on specific areas in a landscape this large. In 2017, while there were no significant peaks in the BUI, local conditions in the Upper Yukon zone in northeast Alaska were significantly warmer and drier. Consistent with the Upper Yukon BUI trend (Fig. SB5.4), the fire season was extended and fairly severe in that large region of the state, with periods of high fire danger (BUI ≥ 80) from mid-June to mid-August near and north of the Arctic Circle. More than 160 000 ha (63% of the 2017 Alaska total) burned in the Upper Yukon area during this period.

Under a range of climate change scenarios, analyses using multiple approaches project significant increases (up to four-fold) in area burned in high latitude ecosystems by the end of the 21st century (French et al. 2015; Young et al. 2017; Yue et al. 2015, and references therein). In addition, annual lightning frequency is projected to increase by 12% \pm 5% per $^{\circ}\text{C}$ of warming in the contiguous United States (Romps et al. 2014) and may increase correspondingly in high latitudes. Because specific fire events depend on multiple interacting factors, the resulting changes in high latitude fire regimes will vary greatly over space and time, but all evidence indicates that northern ecosystems will become increasingly susceptible to burning.

changes in winter weather, specifically reductions in snow cover areal extent due to winter warming events, which left the ground exposed to subsequent freezing and desiccation (Vikhamar-Schuler et al. 2016). Insect outbreaks were identified as a secondary contributor to vegetation mortality (Bjerke et al. 2017).

i. Terrestrial snow cover in the Arctic—C. Derksen, R. Brown, L. Mudryk, K. Luojus, and S. Helfrich

Satellite-derived estimates of snow cover extent (SCE) over Arctic land areas date back to 1967 and have revealed dramatic reductions since 2005. These changes are important to the Arctic system because spring snow cover over land areas significantly influences the surface energy budget (snow is highly reflective of incoming solar energy), ground thermal regime (snow is an effective insulator of the underlying soil), and hydrological processes (the snowpack stores water in solid form for many months before spring melt). Changes in snow cover also have the potential to impact fauna living above, in, and under the snowpack, vegetation, biogeochemical activity, and exchanges of carbon dioxide and other trace gases (Brown et al. 2017).

Spring (April–June) SCE anomalies for the Arctic (land areas north of 60°N) were regionally computed for North America and Eurasia using the NOAA snow chart climate data record, which extends from 1967 to present (maintained at Rutgers University; Estilow

et al. 2015; <http://climate.rutgers.edu/snowcover/>; Fig. 5.23). For the first time in over a decade, 2017 Eurasian Arctic spring SCE was above average relative to the 1981–2010 reference period. April and May SCE anomalies were positive, including the second highest May SCE over the period of satellite observations. These are the first positive SCE anomalies observed in May over the Eurasian Arctic since 2005; June SCE anomalies were positive across the Eurasian Arctic for the first time since 2004. SCE anomalies over the North American Arctic were negative all spring but did not approach the series of record-breaking low SCE values observed in recent years.

Snow cover duration (SCD) departures were calculated from the NOAA Interactive Multisensor Snow and Ice Mapping System (IMS; Helfrich et al. 2007) product to identify differences in the onset of snow cover in fall and melt of snow cover in spring relative to a 1998–2010 reference period. While there was evidence of earlier snow cover onset over much of midlatitude Eurasia in autumn 2016 (consistent with cold surface air temperature anomalies), Arctic land areas (with the exception of Alaska) had near-normal snow onset timing (Fig. 5.24a). Later-than-normal snow melt onset across Eurasia (Fig. 5.24b), also reflected in the positive SCE anomalies (Fig. 5.23), was consistent with colder-than-normal surface air temperatures across this region (especially in May and June). Spring snow melt across the Canadian

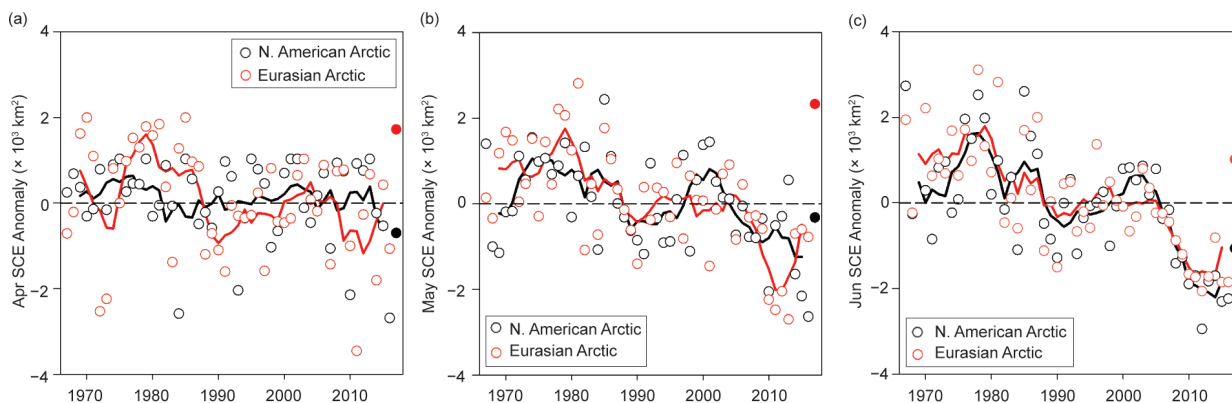


FIG. 5.23. (a) Monthly SCE anomaly ($\times 10^3 \text{ km}^2$) for Arctic land areas ($> 60^\circ\text{N}$) from the NOAA snow chart CDR for (a) Apr, (b) May, and (c) Jun from 1967 to 2017. Anomalies are relative to the average for 1981–2010 and standardized (each observation is differenced from the mean and divided by the standard deviation and is thus unitless). Solid black and red lines depict 5-yr running means for North America and Eurasia, respectively. Solid symbols denote anomalies for 2017.

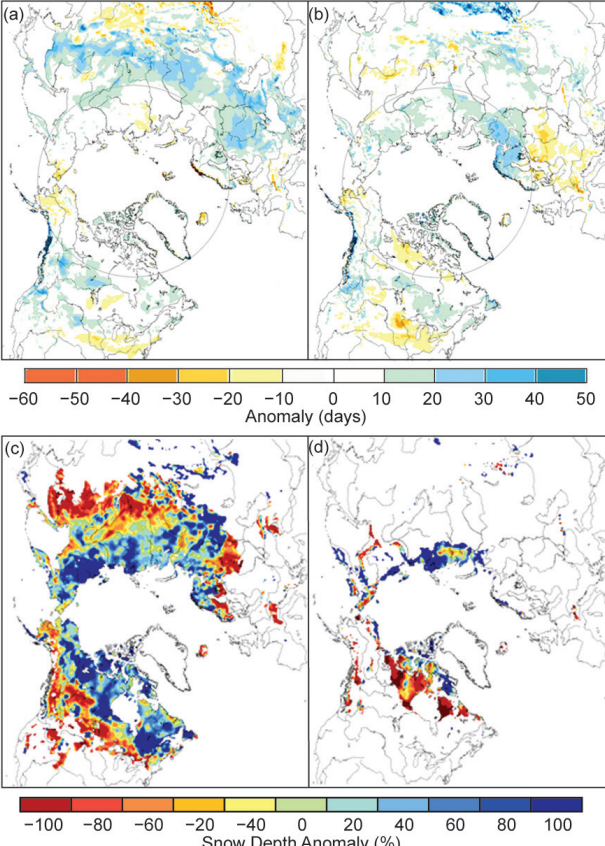


FIG. 5.24. SCD anomalies (%) from the NOAA daily IMS snow cover product (Helfrich et al. 2007; relative to 1998–2010 base period because of the shorter available time series but higher spatial resolution IMS data). IMS data record for the (a) 2016 autumn season and (b) 2017 spring season. Snow depth anomaly (% of 1999–2010 average) from the CMC snow depth analysis for (c) Apr and (d) Jun 2017.

Arctic was slightly earlier than normal, coincident with warmer-than-average surface temperatures in May and June. Snow depth anomalies derived from the Canadian Meteorological Centre daily gridded global snow depth analysis (Brasnett 1999) showed predominantly positive anomalies over high latitude regions of Siberia and North America in April (Fig. 5.24c) and mainly negative anomalies outside the Arctic. By late spring (June), the anomalies exhibited contrasting continental patterns, with Eurasia characterized by extensive positive snow depth anomalies, while the North American Arctic was dominated by negative snow depth anomalies (Fig. 5.24d), consistent with the region of earlier snow melt (Fig. 5.24b).

Four independent products were integrated to generate a multidataset snow water equivalent (SWE; the amount of water stored in solid form as snow) anomaly time series (1980–2017) for April (typically the month of maximum SWE across the Arctic; Fig. 5.25). The datasets were derived from: (1) modern atmospheric reanalysis (the Modern-Era Retrospective Analysis for Research and Applications version 2; Reichle et al. 2017); (2) reconstructed SWE driven by ERA-Interim meteorology described by Brown et al. (2003); (3) the physical snowpack model Crocus driven by ERA-Interim meteorology (Brun et al. 2013); and (4) the European Space Agency GlobSnow product derived through a combination of satellite passive microwave measurements and climate station observations (Takala et al. 2011). While there is a high degree of interannual variability in the multidataset SWE anomalies, they predominantly show a negative trend since 2000 (Fig. 5.25). North American Arctic SWE was again negative in 2017 while Eurasian SWE anomalies were positive, indicating a deeper-than-

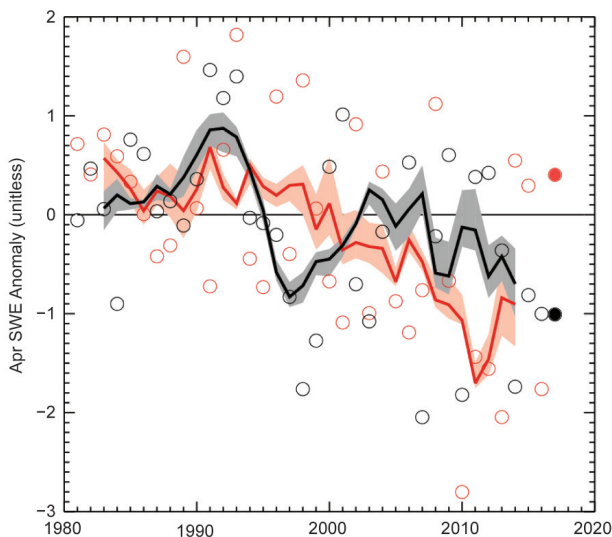


FIG. 5.25. Mean Apr SWE anomalies for Arctic land areas calculated from four independent products for North American (black) and Eurasian (red) sectors of the Arctic. Anomalies are relative to the average for 1981–2010 and standardized (each observation is differenced from the mean and divided by the std. dev. and is thus unitless). Solid black and red lines depict 5-yr running means for North America and Eurasia, respectively, and shading indicates the interdataset anomaly spread (± 1 std. dev.). Solid symbols denote anomalies for 2017.

average snowpack in early spring was a precursor to the above-average snow extent that followed later in the season.

Despite the long-term decline in Arctic spring SCE driven by increasing temperature trends, negative snow anomalies are not consistently observed in every season (nor in all regions). Off-trend anomalies, such as those observed in the Eurasian Arctic in 2017, are driven by natural variability in atmospheric circulation patterns which drive regional temperature and precipitation anomalies. The rebound in Eurasian SCE during May and June 2017 was consistent with winter and spring season circulation patterns which generally favored colder surface temperatures, enhanced precipitation, and above-average snow accumulation across northern Eurasia.

j. Ozone and UV radiation—G. H. Bernhard, V. E. Fioletov, J.-U. Groöb, I. Ialongo, B. Johnsen, K. Lakkala, G. L. Manney, and R. Müller

This report emphasizes the November 2016 to April 2017 period because chemically-induced loss of polar ozone occurs predominantly during winter and spring (WMO 2014). Chemical processes that drive ozone depletion are initiated at temperatures below about 195K (-78°C) in the lower stratosphere

(altitude of approximately 15 to 25 km), which lead to the formation of polar stratospheric clouds (PSCs). These clouds act as a catalyst to transform inactive forms of chlorine-containing substances (e.g., HCl and ClONO₂) to active, ozone-destroying chlorine species (e.g., ClO).

Temperatures in the Arctic stratosphere between late November and late December 2016 were about 5°C higher than the average temperature of the observational record (1979–2015); temperatures in late November 2016 were near the highest values on record for this period. Temperatures dropped below the threshold for the formation of PSCs only in late December. (The onset of PSC formation is typically in early December with the earliest onsets observed in mid-November.) Temperatures remained low enough to sustain PSCs through mid-February 2017. Starting in late December, modest chlorine activation was measured by the *Aura* Microwave Limb Sounder (MLS). From late January to mid-February 2017, active chlorine (ClO) concentrations were, on average, 45% higher than the mean concentration calculated from the MLS data record (2005–16) because stratospheric temperatures during this period were about 4°C below average. Ozone decreases via destruction by activated chlorine started in late January and continued through mid-March 2017. After mid-March, chlorine was deactivated and chemical ozone destruction ceased.

Between December 2016 and mid-January 2017, ozone mixing ratios (a measure of ozone concentrations) were close to the upper limit of values from the observational record (2004–17) (Fig. 5.26). At the end of January, mixing ratios started to decline and fell below average in March and April 2017. However, in

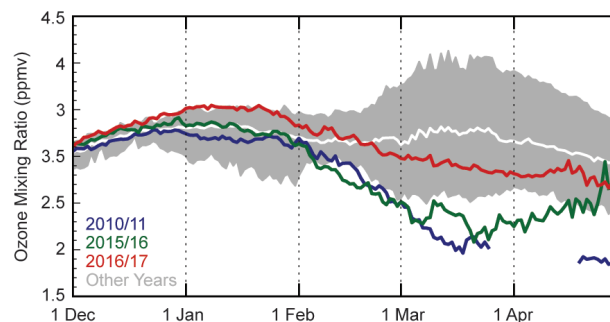


FIG. 5.26. Average ozone mixing ratios (ppmv) measured by *Aura* MLS at an altitude of ~18 km for the area bounded by the polar vortex. Data from 2016/17 (red), 2015/16 (green), and 2010/11 (blue) are compared with the average (solid white) and minimum/maximum range (gray shading) from 2004/05 to 2014/15, excluding 2010/11. Gaps in the record for 2010/11 are due to missing data.

comparison to 2010/11 and 2015/16 (the years with the largest chemical ozone loss in the observational record), mixing ratios in 2016/17 remained well above values observed in those record years.

The evolution of the Arctic total ozone column (TOC; i.e., ozone amounts integrated from the surface to the top of the atmosphere) is used here to compare 2017 measurements to the observational record (1979–2016). Specifically, March TOC is evaluated because chemically induced Arctic ozone loss is typically largest in this month (WMO 2014). The minimum Arctic daily TOC measured by satellites in March 2017 was 345 Dobson units (DU), which was 7.7% (29 DU) below the average of the observational record (374 DU) and 5.4% (20 DU) below the 2005–16 average when MLS data are also available (Fig. 5.27).

Spatial deviations of monthly average TOCs from historical (2005–16) averages (Figs. 5.28a,b) were estimated with measurements from the Ozone Monitoring Instrument (OMI), which is co-located with MLS on the *Aura* satellite. Average TOCs for March 2017 were up to 15% higher over the Norwegian Sea, Greenland, and northern Canada, and up to 20% lower over northern Siberia relative to the long-term average (Fig. 5.28a). This spatial pattern is similar to a recently described Eurasia–North America dipole mode for the month of February, consisting of a shift to negative ozone anomalies over Eurasia and positive anomalies over North America (Zhang et al. 2018). Monthly average TOCs for April 2017, the month when the polar vortex (the low-temperature cyclone in which most of the springtime chemical destruction

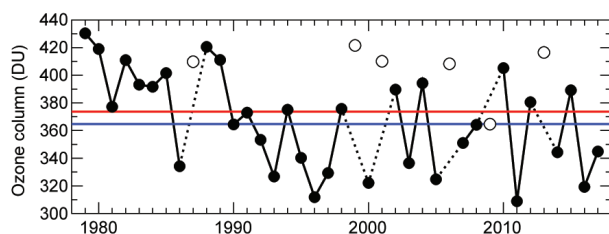


FIG. 5.27. Area-averaged minimum total ozone column (DU) for Mar that are calculated poleward of 63° equivalent latitude (Butchart and Remsburg 1986). Open circles represent years in which the polar vortex broke up before Mar, resulting in relatively high values due to mixing with lower latitude air masses and a lack of significant chemical ozone depletion. Red and blue lines indicate the average TOC for 1979–2016 and 2005–16, respectively. Data are adapted from Müller et al. (2008) and WMO (2014), updated using ERA-Interim reanalysis data (Dee et al. 2011a). Ozone data from 1979–2012 are based on the combined total column ozone database version 3.0 produced by Bodeker Scientific (www.bodekerscientific.com/data/total-column-ozone). Data for 2013–17 are from OMI.

of ozone occurs) broke up and air from high and mid-latitudes started to mix, departed by less than $\pm 10\%$ from the historical average, and ozone anomalies for May through November 2017 were unremarkable.

UV radiation is quantified with the UV index (UVI), which is a measure of the ability of UV radiation to cause erythema (sunburn) in human skin (WHO 2002). In addition to its dependence on TOC, the UVI depends on the sun angle, cloud cover, and surface albedo (Weatherhead et al. 2005). In the Arctic, the UVI scale ranges from 0 to about 7, with sites closest to the North Pole having the smallest peak radiation and UVI values < 4 all year. UVI values ≤ 5 indicate low to moderate risk of erythema (WHO 2002). UVI anomalies are assessed using satellite instruments (OMI) and ground-based measurements, with the former providing the better spatial coverage and the latter providing greater regional accuracy (Bernhard et al. 2015). Figures 5.28c,d quantify the spatial differences in monthly average noontime UVIs from historical (2005–16) averages and are based on OMI measurements. Figures 5.28c,d also indicate anomalies calculated from ground-based measurements at ten research stations located throughout the Arctic and Scandinavia.

Compared to the historical mean, average noontime UVIs for March 2017 were larger by up to 25% over northern Siberia and smaller by up to 20% over Greenland and the Davis Strait (Fig. 5.28c). Areas with high UVIs roughly match areas with low TOCs and vice versa, but UVI anomalies have a larger spatial variability because of their added dependence on cloud cover. While relative UVI anomalies can be high, absolute anomalies remained below 1 UVI unit because solar elevations in March in the Arctic remain low. Anomalies derived from OMI and ground-based measurements agree to within $\pm 7\%$. Anomalies for April 2017 differed by less than $\pm 15\%$ from the historical average (not shown), except at the western coast of Alaska and the Bering Strait, where OMI measured anomalies of up to 50%.

Ground-based UV measurements at all sites varied within historical bounds from July to November. However, UVIs at Alert, Eureka, and Resolute in northernmost Canada and at Summit, Greenland, were unusually high between 15 May and 15 June despite only small negative TOC anomalies (Fig. 5.28b). At Alert, Resolute, and Summit, positive UVI anomalies of between 5% and 10% measured at the ground were in good ($\pm 3\%$) agreement with the satellite data. At Eureka, heavy snowfall in mid-May led to high surface albedo and high UVIs until mid-June. Measurements from the ground indicated a positive

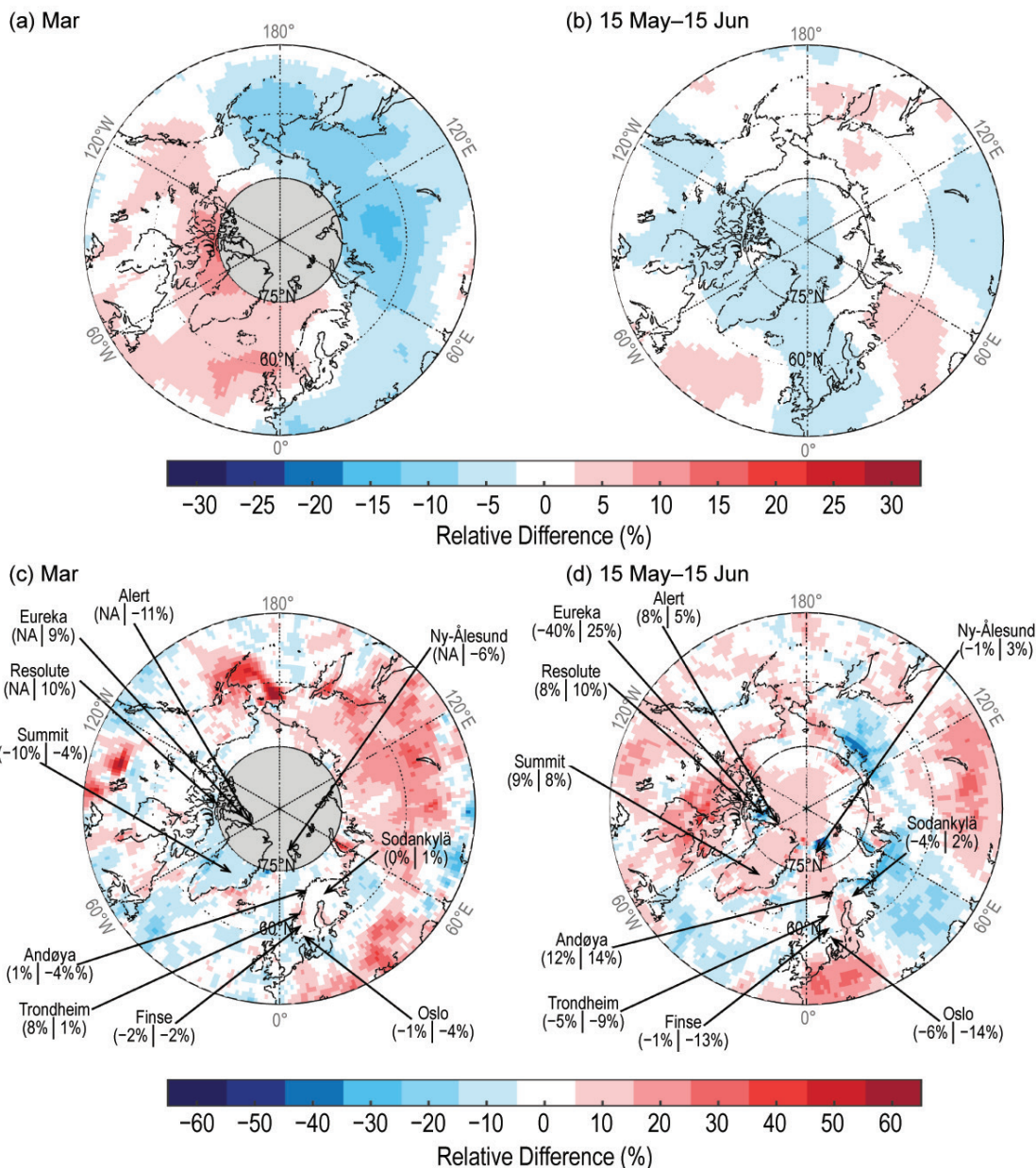


FIG. 5.28. (a) Anomalies of TOC (%) and (c) noontime UVI (%) for Mar 2017. (b) and (d) as in (a) and (c) but for 15 May–15 Jun. Anomalies are relative to 2005–16 averages. Maps are based on OMT03 Level 3 total ozone product (Bhartia and Wellemeyer 2002). (c) and (d) also compare UVI anomalies from OMI (first value in parenthesis) with ground-based measurements at 10 locations (second value presented). Gray shading indicates areas where no OMI data are available.

UVI anomaly of 25%, while OMI reported a negative anomaly of -40%. This large inconsistency can be attributed to systematic errors in the OMI dataset, which are caused by a mismatch of the actual high surface albedo and the albedo climatology (Tanskanen et al. 2003) used by the OMI UV algorithm. Because of this mismatch, the high reflectivity observed from space due to snow was misinterpreted as cloud cover, resulting in erroneously low UVIs reported by OMI. The relatively large difference (12%) of UVI

anomalies derived from OMI and ground-based measurements at Finse, Norway, for the same period can be attributed to snow cover disappearing 20 days earlier in 2017 compared with the average snow disappearance date for 2005–16 (Fig. 5.28d). Differences between satellite and ground-based measurements from space require verification with ground-based measurements, in particular during months when snowmelt occurs.

